A physically-based mixed hardening model for the prediction of the ductility limits of thin metal sheets using a CPFE approach

S. Zhou, M. Ben Bettaieb [*], F. Abed-Meraim

Université de Lorraine, CNRS, Arts et Métiers Institute of Technology, LEM3, F-57070 Metz, France
DAMAS, Laboratory of Excellence on Design of Alloy Metals for low-mAss Structures, Université de Lorraine, France

ABSTRACT

Keywords:
Dislocation density
Kinematic hardening
Crystal plasticity
Stability and bifurcation
Forming limit diagrams

An advanced Crystal Plasticity Finite Element (CPFE) approach is developed to accurately predict the ductility limit strains of thin metal sheets. This method uses polycrystalline unit cells to represent the metal sheets at the macroscopic level. The macroscopic behavior of these unit cells is determined based on that of the constituent single crystals using the periodic homogenization multiscale scheme. At the single crystal scale, the constitutive framework follows a finite strain rate-independent formulation, with the flow rule governed by the Schmid law. The evolution of the single crystal yield surface is described through a physically-based mixed hardening model, where isotropic hardening is characterized by a dislocation density-based formulation, while kinematic hardening is described by the nonlinear Armstrong–Frederick model. The unit cell ductility limit strains are predicted by the Rice bifurcation criterion. The reliability of the mixed hardening model in accurately reproducing mechanical behavior is confirmed through simulations of uniaxial tension/compression loading. Then, the developed computational strategy is used to investigate the impact of key microstructural hardening parameters on the initiation of localized necking under linear strain paths. The numerical predictions reveal the significant influence of these parameters on the formability of thin metal sheets. Additionally, the analysis of ductility limits under non-linear strain paths demonstrates a strong dependency of the numerical predictions on strain path changes. The numerical predictions obtained by the developed CPFE multiscale strategy are compared with experimental results from the literature. In summary, the proposed approach provides a reliable tool for accurately predicting the ductility limits of thin metal sheets, offering valuable insights for engineering applications.

1. Introduction

A deep understanding of the mechanical properties of metal alloys during plastic deformation, including work-hardening and plastic anisotropy, is crucial for metallurgists and designers seeking to enhance the ductility of their products. Ductility is usually limited by the development of plastic instability resulting in strain localization. The ductility limits are often characterized using the concept of forming limit diagrams (FLDs), initially introduced by Keeler and Backhofen (1963) and subsequently refined by Goodwin (1968). Traditionally, the determination of these FLDs involves numerical approaches that rely on the combination of a constitutive framework and a strain localization criterion. The adopted constitutive frameworks are generally categorized into two families: classical phenomenological constitutive models and multiscale schemes.

In the context of phenomenological constitutive frameworks, isotropic hardening has been most widely used to model the hardening behavior of metal sheets. Several contributions, such as Hutchinson and Neale (1978) and Ben Bettaieb and Abed-Meraim (2015), have extensively analyzed the effect of isotropic hardening parameters on the shape and level of FLDs. More recently, Bonatti and Mohr (2021) have used a neural network model to assess the impact of bi-linear strain paths on the FLDs predicted by the M–K criterion (Marciniak and Kuczyński, 1967). In these studies, basic isotropic hardening laws have been used to characterize work hardening. However, more advanced isotropic hardening models, such as the microstructural-based hardening model developed by Teodosiu and Hu (1995, 1998), have gained attention for predicting ductility limits. Notably, Haddag et al. (2009) and Butuc et al. (2011) have adopted the Teodosiu and Hu hardening model to predict the forming limit diagrams of DP and DC steel sheets, respectively. These investigations have consistently demonstrated that ductility limits increase with the strain hardening rate ($= d\sigma/d\varepsilon$). To provide a more accurate description of hardening phenomenon, kinematic hardening is usually incorporated into the constitutive models. Accounting for kinematic hardening becomes essential for accurate predictions of the mechanical behavior and, consequently, the ductility limits of various metallic materials. The consideration of kinematic hardening is crucial for capturing important physical phenomena, such as Bauschinger and ratcheting effects, which remain unaccounted for otherwise. In previous studies, such as Ben Bettaieb and Abed-Meraim (2017a,b), the impact of kinematic hardening on the onset of localized necking has been thoroughly analyzed by using the Prager and Armstrong–Frederick (Armstrong and Frederick, 1966) models for the description of the backstress evolution. The results of these studies confirm that the predicted formability limits depend on the involved kinematic hardening model, although the magnitude of changes in ductility limits (either increase or decrease) remains relatively small. Furthermore, these findings emphasize that the effect of kinematic hardening on the ductility limits is highly dependent on the applied strain path.

Despite their computational efficiency and ease of numerical implementation, phenomenological models often fall short in accurately capturing essential physical and microstructural features, such as dislocation motion, plastic anisotropy induced by both morphological and crystallographic texture, microscopic heterogeneity, and grain boundaries. To address these limitations, several multiscale approaches have been developed to predict the deformation behavior and ductility limits of polycrystalline metals. In these multiscale schemes, the mechanical behavior is typically modeled at the single crystal level, and a multiscale transition scheme is used to predict the macroscopic mechanical behavior based on the properties of the individual single crystals. The majority of crystal plasticity constitutive frameworks established and used in the literature only consider the isotropic hardening phenomenon (see, for example, Ben Bettaieb et al. 2012, Akpama et al. 2016, 2017, Zhu et al. 2023a,b ...), while the link between hardening and most relevant microscopic phenomena and parameters (such as dislocation motion and saturation) is not very clear and explicit. To address the latter limitation, physically-based isotropic hardening models have been developed to characterize plastic deformation at the single crystal level by considering the microstructural state of materials. These models incorporate material parameters with a well-defined physical interpretation. For instance, Kocks (1976) has proposed a hardening model based on dislocation density, where the evolution rule for dislocation density is described by storage and annihilation processes. Recently, Mohammadnejad et al. (2021) have studied the influence of dislocation density on FLDs using the Taylor homogenization scheme coupled with the M–K approach (Marciniak and Kuczyński, 1967). They found that the predicted formability limits are closer to the experimental measurements when a dislocation density-based hardening model is considered. The Taylor model assumes that all the single crystals composing the polycrystalline aggregate experience the same strain field as the macroscopic one. Furthermore, the interactions between grains are not considered in the Taylor model. Consequently, the use of the Taylor model leads to some conceptual inaccuracies in predicting the overall mechanical behavior of polycrystalline aggregates and fails to satisfy the equilibrium conditions within the multiscale framework. To address these issues, the mean-field self-consistent scheme has been developed to provide a more comprehensive description of the evolution of microscopic fields and to ensure the full respect of the equilibrium conditions. Furthermore, within this multiscale scheme, each grain is assumed to be ellipsoidal, thus allowing a slightly better description of the grain morphology compared to the Taylor model. The self-consistent approach has been coupled in Franz et al. (2013) with the Rice bifurcation theory (Rice, 1976) to study the influence on the predicted ductility limits of various microstructural hardening parameters, such as the initial value of the critical resolved shear stress (CRSS), the dislocation storage and annihilation parameters. The predictions presented in Franz et al. (2013) reveal that the microstructural parameters significantly affect the ductility of single crystals and polycrystalline aggregates.

However, mean-field homogenization schemes are often limited in accurately modeling the mechanical behavior of polycrystalline aggregates. In fact, mean-field schemes are not fully capable of considering more complex grain morphologies as well as the heterogeneity of the mechanical fields inside the same grain. Furthermore, the conditions applied on the boundaries of the polycrystalline aggregates are not accurately considered within mean-field approaches. To remedy these limitations, full-field homogenization schemes have been established in the literature. These schemes rely either on the finite element method (FEM) (Kim et al., 2017; Bong et al., 2020; Bong and Lee, 2021; Zhu et al., 2023a), or on the fast Fourier transform (FFT) technique (Gupta et al., 2018; Nagra et al., 2018; Han et al., 2020). Within these frameworks, microscopic strain and stress fields arising from the collective motions of dislocations can be accurately predicted, offering a more comprehensive understanding of the deformation behavior of polycrystalline aggregates. The Crystal Plasticity Finite Element Method (CPFEM) has been proven to be a powerful tool for studying plastic behavior of thin metal sheets, such as formability (Kim et al., 2017; Bong et al., 2020; Bong and Lee, 2021). In Bong and Lee (2021), CPFEM has been coupled with the M–K approach to predict the formability of ultra-thin ferritic stainless steels. In their study, the initial imperfection has been taken to be mainly due to surface roughening, and only isotropic hardening has been considered, where a dislocation density-based law has been used to model the evolution of the single crystal yield surface. Numerous experimental and numerical investigations have revealed that the deformation heterogeneity inside the aggregate and the different grain crystallographic orientations may induce significant backstress, which must be accounted for in

microscopic constitutive modeling (Brahme et al., 2011). To this end, Harder (1999) has introduced a dislocation density-based hardening model that incorporates the backstress evolution. This model has been used to predict the influence of the Bauschinger effect on macroscopic behavior. More recent studies have adopted kinematic hardening modeling to numerically investigate the occurrence of fatigue (Le Pécheur et al., 2012; Lu et al., 2016; Zhou et al., 2022), ratcheting (Dong et al., 2014; Hennessey et al., 2017; Dong et al., 2020; Farooq et al., 2020), and macroscopic response (Agaram et al., 2021) in polycrystalline aggregates under strain-controlled cyclic loadings. To the best knowledge of the authors, kinematic hardening crystal plasticity models have not yet been integrated into a CPFE strategy to predict the ductility limits of polycrystalline aggregates.

The ultimate goal of this study is to predict ductility limits using the CPFE approach, with a special emphasis on assessing the influence of physical parameters associated with dislocation density-based isotropic and kinematic hardening models. To achieve this goal, a unit cell, assumed to be representative of the studied material, is generated by NEPER software (Quey et al., 2011) based on the Voronoi tessellation technique. Subsequently, the unit cell is discretized into a large number of finite elements, and each integration point of the finite elements is treated as a single crystal. The same crystallographic orientation is assigned to all the single crystals belonging to the same grain. The crystallographic texture is generated using ATEX software (Beausir and Fundenberger, 2017), and the periodic homogenization technique (Zhu et al., 2020b,a, 2023b) is adopted to derive the macroscopic characteristics of the unit cell from those of the individual single crystals. The Python script HOMTOOLS, developed by Lejeunes and Bourgeois (2011), is used to ensure the prescription of the periodic boundary conditions (PBCs) and the application of the macroscopic loading for FLD predictions. For the latter purpose, the unit cell is subjected to biaxial loadings, spanning from uniaxial tension to equibiaxial tension states. The single crystal constitutive equations follow a finite strain rate-independent framework with physically-based isotropic-kinematic hardening. Isotropic hardening obeys the Kocks dislocation density law (Kocks, 1976), while kinematic hardening is modeled by the typical nonlinear A–F law (Armstrong and Frederick, 1966). The flow behavior follows the classical Schmid law, and the onset of macroscopic strain localization is detected by the Rice bifurcation criterion. The Rice bifurcation approach presents some key advantageous compared to other localized necking criteria. Indeed, besides its sound mathematical foundations, the bifurcation approach does not require any fitting parameter, such as the initial imperfection factor needed in the M–K analysis. Furthermore, compared to the initial imperfection approach, the use of the bifurcation theory allows a considerable reduction in the CPU time required for the determination of a complete FLD (Akpama et al., 2017). A set of Python scripts, based on the condensation technique (Zhu et al., 2022), is used to determine the macroscopic acoustic tensor from the global stiffness matrix. This macroscopic acoustic tensor is required to perform the bifurcation analysis. The validity of the implemented dislocation density-based isotropic-kinematic hardening model is checked through simulations of cyclic tension/compression tests. Furthermore, the effect of different hardening models and their respective parameters on ductility limits is thoroughly examined under linear strain paths. Ductility limits under non-linear strain paths are also investigated using the physically-based isotropic-kinematic hardening model, where these non-linear loading paths are composed of two sequential linear strain paths. It is worth noting that our simulation results align with those reported in Yang et al. (2010), Butuc et al. (2011), Ma et al. (2018) and Qin et al. (2018). On the other hand, the predicted ductility limits are compared with those obtained from the well-known full-constraint Taylor model. Moreover, the limit strain predictions obtained by the current computational strategy are compared with the experimental results reported in Nicoletti et al. (2023). Ultimately, an actual material texture is considered to investigate the effect of the initial crystallographic texture on the predicted ductility limits.

The structure of this paper is arranged as follows:

- Section 2 outlines the physically-based isotropic-kinematic hardening models, their integration within the rate-independent crystal plasticity framework, and the corresponding integration algorithm. It also briefly explains the main concepts of the periodic homogenization method and the Rice bifurcation theory.
- In Section 3, the ductility limit predictions are determined for different hardening models, and the effects of physical factors and parameters on ductility limits are discussed.
- Section 4 summarizes the main findings of the current study.

2. Theoretical framework and numerical implementation

2.1. Single crystal plasticity constitutive equations

The single crystal mechanical behavior follows a finite strain elastoplastic framework. As a result, the total microscopic elastoplastic deformation gradient $\mathbf{f}$ can be multiplicatively decomposed into its elastic $\mathbf{f}^e$ and plastic $\mathbf{f}^p$ parts, as shown in Fig. 1:

$$\mathbf{f} = \mathbf{f}^e \cdot \mathbf{f}^p. \tag{1}$$

The elastic part $\mathbf{f}^e$ can be further decomposed into a stretching tensor $\mathbf{v}^e$ and a rotation tensor $\bar{\mathbf{r}}$:

$$\mathbf{f}^e = \mathbf{v}^e \cdot \bar{\mathbf{r}}. \tag{2}$$

In most metallic materials, it is commonly assumed that the elastic deformation is considerably smaller in magnitude compared to the plastic deformation. Therefore, tensor $\mathbf{v}^e$ is very close to the second-order identity tensor ($\mathbf{v}^e \approx \mathbf{I}_2$). As to the rotation tensor $\bar{\mathbf{r}}$,

it defines the single crystal orientation with respect to the deformed configuration, and is typically expressed in terms of the Euler angles (φ_1, ϕ, φ_2), as follows:

$$\bar{\mathbf{r}} = \begin{bmatrix} cos\varphi_1 cos\varphi_2 - sin\varphi_1 sin\varphi_2 cos\phi & sin\varphi_1 cos\varphi_2 + cos\varphi_1 sin\varphi_2 cos\phi & sin\varphi_2 sin\phi \\ -cos\varphi_1 sin\varphi_2 - sin\varphi_1 cos\varphi_2 cos\phi & -sin\varphi_1 sin\varphi_2 + cos\varphi_1 cos\varphi_2 cos\phi & cos\varphi_2 sin\phi \\ sin\varphi_1 sin\phi & -cos\varphi_1 sin\phi & cos\phi \end{bmatrix}. \tag{3}$$

For efficient numerical treatment, the single crystal constitutive equations are defined using an Eulerian formulation. Under this formulation, the single crystal velocity gradient $\mathbf{g} = \dot{\mathbf{f}} \cdot \mathbf{f}^{-1}$ is classically adopted as an appropriate measure of the deformation rate. Considering the earlier assumption made on the stretching tensor $\mathbf{v}^e$, the velocity gradient $\mathbf{g}$ can be additively decomposed into its symmetric part $\mathbf{d}$ and anti-symmetric part $\mathbf{w}$ as follows:

$$\begin{aligned} \mathbf{g} &= \dot{\mathbf{f}}^e \cdot \mathbf{f}^{e-1} + \mathbf{f}^e \cdot \dot{\mathbf{f}}^p \cdot \mathbf{f}^{p-1} \cdot \mathbf{f}^{e-1}; \\ &= \dot{\mathbf{v}}^e + \dot{\bar{\mathbf{r}}} \cdot \bar{\mathbf{r}}^T + \bar{\mathbf{r}} \cdot \dot{\mathbf{f}}^p \cdot \mathbf{f}^{p-1} \cdot \bar{\mathbf{r}}^T; \\ &= \mathbf{d} + \mathbf{w}, \end{aligned} \tag{4}$$

where the symmetric part $\mathbf{d}$ (resp. anti-symmetric part $\mathbf{w}$) can be further decomposed into an elastic part $\mathbf{d}^e$ (resp. $\mathbf{w}^e$) and a plastic part $\mathbf{d}^p$ (resp. $\mathbf{w}^p$):

$$\mathbf{d} = \frac{1}{2}(\mathbf{g} + \mathbf{g}^T) = \mathbf{d}^e + \mathbf{d}^p; \quad \mathbf{w} = \frac{1}{2}(\mathbf{g} - \mathbf{g}^T) = \mathbf{w}^e + \mathbf{w}^p,$$

with $\quad \mathbf{d}^e = \dot{\mathbf{v}}^e; \quad \mathbf{d}^p = \bar{\mathbf{r}} \cdot (\dot{\mathbf{f}}^p \cdot \mathbf{f}^{p-1})_{sym} \cdot \bar{\mathbf{r}}^T; \quad \mathbf{w}^e = \dot{\bar{\mathbf{r}}} \cdot \bar{\mathbf{r}}^T; \quad \mathbf{w}^p = \bar{\mathbf{r}} \cdot (\dot{\mathbf{f}}^p \cdot \mathbf{f}^{p-1})_{asym} \cdot \bar{\mathbf{r}}^T. \tag{5}$

Plastic deformation is assumed to be solely driven by crystallographic slip on the slip systems. Therefore, the plastic contribution of the velocity gradient $\mathbf{g}$ can be expressed as follows:

$$\mathbf{d}^p + \mathbf{w}^p = \sum_{\alpha=1}^{N_s} \dot{\gamma}^\alpha \left(\vec{\mathbf{m}}^\alpha \otimes \vec{\mathbf{n}}^\alpha \right) = \sum_{\alpha=1}^{N_s} \dot{\gamma}^\alpha \mathbf{M}^\alpha, \tag{6}$$

where:

- N_s is the number of physical slip systems (equals to 12 for FCC crystal slip systems),
- $\dot{\gamma}^\alpha$ represents the slip rate on the slip system α,
- $\vec{\mathbf{m}}^\alpha$ designates the slip direction vector and $\vec{\mathbf{n}}^\alpha$ is the vector normal to the slip plane.
- $\mathbf{M}^\alpha$ is the Schmid tensor equals to the tensor product $\vec{\mathbf{m}}^\alpha \otimes \vec{\mathbf{n}}^\alpha$.

For practical reasons, each slip system is decomposed into two opposite oriented slip systems, denoted as $(\vec{\mathbf{m}}^\alpha, \vec{\mathbf{n}}^\alpha)$ for slip systems $\alpha = 1, \ldots, N_s$ and $(-\vec{\mathbf{m}}^{\alpha-N_s}, \vec{\mathbf{n}}^{\alpha-N_s})$ for slip systems $\alpha = N_s + 1, \ldots, 2N_s$. This decomposition is adopted to manage only positive values of slip rates. To simplify the subsequent equations, we introduce the tensors $\mathbf{R}^\alpha$ and $\mathbf{S}^\alpha$ defined as:

$$\mathbf{R}^\alpha = \frac{1}{2} \left(\vec{\mathbf{m}}^\alpha \otimes \vec{\mathbf{n}}^\alpha + \vec{\mathbf{n}}^\alpha \otimes \vec{\mathbf{m}}^\alpha \right); \quad \mathbf{S}^\alpha = \frac{1}{2} \left(\vec{\mathbf{m}}^\alpha \otimes \vec{\mathbf{n}}^\alpha - \vec{\mathbf{n}}^\alpha \otimes \vec{\mathbf{m}}^\alpha \right). \tag{7}$$

Hence, the plastic strain rate $\mathbf{d}^p$ and plastic spin $\mathbf{w}^p$ can be reformulated in terms of $\mathbf{R}^\alpha$ and $\mathbf{S}^\alpha$ as follows:

$$\mathbf{d}^p = \sum_{\alpha=1}^{2N_s} \dot{\gamma}^\alpha \mathbf{R}^\alpha; \quad \mathbf{w}^p = \sum_{\alpha=1}^{2N_s} \dot{\gamma}^\alpha \mathbf{S}^\alpha. \tag{8}$$

The rotation tensor $\bar{\mathbf{r}}$ defined in Eq. (3) is chosen such that the counterpart $\vec{\mathbf{m}}_0^\alpha$ (resp. $\vec{\mathbf{n}}_0^\alpha$) of $\vec{\mathbf{m}}^\alpha$ (resp. $\vec{\mathbf{n}}^\alpha$) in the intermediate configuration remains constant during deformation. These constant vectors $\vec{\mathbf{m}}_0^\alpha$ and $\vec{\mathbf{n}}_0^\alpha$ are related to vectors $\vec{\mathbf{m}}^\alpha$ and $\vec{\mathbf{n}}^\alpha$ by the following equations:

$$\vec{\mathbf{m}}^\alpha = \bar{\mathbf{r}} \cdot \vec{\mathbf{m}}_0^\alpha; \quad \vec{\mathbf{n}}^\alpha = \vec{\mathbf{n}}_0^\alpha \cdot \bar{\mathbf{r}}^T, \tag{9}$$

where the components of vectors $\vec{\mathbf{m}}_0^\alpha$ and $\vec{\mathbf{n}}_0^\alpha$ for FCC single crystals are provided in Appendix A. To ensure the objectivity of the single crystal constitutive equations, Eqs. (4), (5) and (6) can be expressed in the crystal lattice frame (intermediate configuration) defined by the rotation tensor $\bar{\mathbf{r}}$ with respect to the current configuration. To simplify the following presentation, tensors and vectors evaluated in the lattice frame are marked with an overline notation ($\bar{\cdot}$). In this frame, the velocity gradient $\bar{\mathbf{g}}$ is given by:

$$\begin{aligned} \bar{\mathbf{g}} &= \bar{\mathbf{r}}^T \cdot \mathbf{g} \cdot \bar{\mathbf{r}} = \bar{\mathbf{d}} + \bar{\mathbf{w}}; \\ &= \bar{\mathbf{d}}^e + \bar{\mathbf{d}}^p + \bar{\mathbf{w}}^e + \bar{\mathbf{w}}^p, \end{aligned} \tag{10}$$

where the plastic parts $\bar{\mathbf{d}}^p$ and $\bar{\mathbf{w}}^p$ of the velocity gradient $\bar{\mathbf{g}}$ can also be expressed in the crystal lattice frame as:

$$\bar{\mathbf{d}}^p = \sum_{\alpha=1}^{2N_s} \dot{\gamma}^\alpha \mathbf{R}_0^\alpha; \quad \bar{\mathbf{w}}^p = \sum_{\alpha=1}^{2N_s} \dot{\gamma}^\alpha \mathbf{S}_0^\alpha; \quad \text{with} \quad \dot{\gamma}^\alpha \geq 0. \tag{11}$$

In the current study, elasticity is assumed to be linear, isotropic, and can be modeled by the classical Hooke law:

$$\dot{\bar{\sigma}} = \bar{\mathbf{c}}^e : \bar{\mathbf{d}}^e = \bar{\mathbf{c}}^e : \left(\bar{\mathbf{d}} - \bar{\mathbf{d}}^p \right), \tag{12}$$

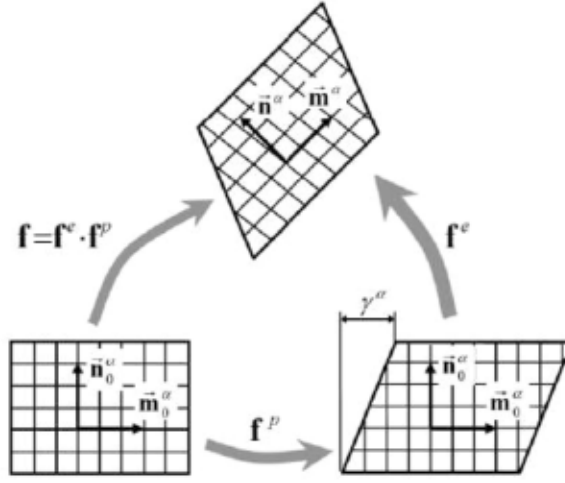**Fig. 1.** Schematic representation of the multiplicative decomposition of the deformation gradient **f** into an elastic contribution **f**^{e} and a plastic contribution **f**^{p} (Akpama et al., 2017).

where $\dot{\bar{\sigma}}$ is the rate of the Cauchy stress σ expressed in the lattice frame, $\bar{c}^e$ represents the fourth-order elastic stiffness tensor, which is determined by the material elasticity parameters E and ν.

The plastic flow rule is modeled by the Schmid law, which states that slip can only occur when the difference between the resolved shear stress τ^α and the backstress X^α on a slip system α reaches a critical threshold τ_c^α. Its mathematical expression is as follows:

$$\forall \alpha = 1, \ldots, 2N_s : \begin{cases} \tau^\alpha - X^\alpha < \tau_c^\alpha & \Rightarrow \dot{\gamma}^\alpha = 0 \\ \tau^\alpha - X^\alpha = \tau_c^\alpha & \Rightarrow \dot{\gamma}^\alpha \geq 0 \end{cases}, \tag{13}$$

wherein the expression of the resolved shear stress τ^α is defined as:

$$\forall \alpha = 1, \ldots, 2N_s : \tau^\alpha = \sigma : \mathbf{R}^\alpha, \tag{14}$$

which can be equivalently expressed using the lattice tensors $\bar{\sigma}$ and $\mathbf{R}_0^\alpha$ as:

$$\forall \alpha = 1, \ldots, 2N_s : \tau^\alpha = \bar{\sigma} : \mathbf{R}_0^\alpha. \tag{15}$$

The Schmid law defined by Eq. (13) can be reformulated as a non-linear complementarity problem (NLCP) to make it more suitable for numerical implementation:

$$\forall \alpha = 1, \ldots, 2N_s : f^\alpha = \tau_c^\alpha - (\tau^\alpha - X^\alpha) \geq 0; \quad \dot{\gamma}^\alpha \geq 0; \quad f^\alpha \dot{\gamma}^\alpha = 0. \tag{16}$$

Following Franz et al. (2013), the critical resolved shear stress τ_c^α is described by an anisotropic hardening law, which is assumed to depend on all of the dislocation densities ρ^β, where ρ^β is the dislocation density associated with the βth slip system:

$$\forall \alpha = 1, \ldots, N_s : \tau_c^\alpha = \tau_c^{\alpha+N_s} = \tau_0 + A\mu b \sqrt{\sum_{\beta=1}^{N_s} h^{\alpha\beta} \left(\rho^\beta + \rho^{\beta+N_s} \right)}, \tag{17}$$

where:

- τ_0 denotes the initial value of critical shear stress,
- A is a material constant,
- μ represents the elastic shear modulus,
- b is the magnitude of the Burgers vector,

- $h^{\alpha\beta}$ is a 12×12 hardening interaction matrix defined as follows (Ben Bettaieb et al., 2012):

$$\forall \alpha, \beta = 1, \ldots, N_s : h^{\alpha\beta} =
\begin{bmatrix}
h_1 & h_2 & h_2 & h_4 & h_5 & h_5 & h_3 & h_5 & h_6 & h_3 & h_6 & h_5 \\
 & h_1 & h_2 & h_5 & h_3 & h_6 & h_5 & h_4 & h_5 & h_6 & h_3 & h_5 \\
 & & h_1 & h_5 & h_6 & h_3 & h_6 & h_5 & h_3 & h_5 & h_5 & h_4 \\
 & & & h_1 & h_2 & h_2 & h_3 & h_6 & h_5 & h_3 & h_5 & h_6 \\
 & & & & h_1 & h_2 & h_4 & h_3 & h_5 & h_5 & h_4 & h_5 \\
 & & & & & h_1 & h_5 & h_5 & h_4 & h_6 & h_5 & h_3 \\
 & & & & & & h_1 & h_2 & h_2 & h_4 & h_5 & h_5 \\
 & & & & & & & h_1 & h_2 & h_5 & h_3 & h_6 \\
 & sym & & & & & & & h_1 & h_5 & h_6 & h_3 \\
 & & & & & & & & & h_1 & h_2 & h_2 \\
 & & & & & & & & & & h_1 & h_2 \\
 & & & & & & & & & & & h_1
\end{bmatrix}. \tag{18}$$

The diagonal component h_1 describes the self-hardening, while the off-diagonal components (from h_2 to h_6) describe the latent hardening on the slip systems. For simplicity, isotropic hardening is considered in this work (i.e., $h_1 = h_2 = h_3 = h_4 = h_5 = h_6 = 1$). The evolution of the dislocation density $\dot{\rho}^\alpha$ is governed by the Kocks law (Kocks, 1976) expressed as:

$$\forall \alpha = 1, \ldots, N_s : \dot{\rho}^\alpha = \dot{\rho}^{\alpha+N_s} = \frac{1}{b} \left(\frac{1}{d} + \frac{\sqrt{\sum_{\beta=1,\beta\neq\alpha}^{N_s} \left(\rho^\beta + \rho^{\beta+N_s} \right)}}{K} - 2y_c \left(\rho^\alpha + \rho^{\alpha+N_s} \right) \right) \left(\dot{\gamma}^\alpha + \dot{\gamma}^{\alpha+N_s} \right), \tag{19}$$

where:

- d denotes the average grain size,
- K is a material parameter representing the dislocation storage,
- y_c stands for the critical annihilation distance of dislocations.

The evolution rule of the critical resolved shear stress $\dot{\tau}_c^\alpha$ can be obtained by differentiating Eq. (17) and combining it with Eq. (19):

$$\forall \alpha = 1, \ldots, N_s : \dot{\tau}_c^\alpha = \dot{\tau}_c^{\alpha+N_s} := \sum_{\beta=1}^{N_s} H^{\alpha\beta} \left(\dot{\gamma}^\beta + \dot{\gamma}^{\beta+N_s} \right),$$

$$\text{with } H^{\alpha\beta} = \frac{A\mu h^{\alpha\beta}}{2\sqrt{\sum_{\xi=1}^{N_s} h^{\alpha\xi} \left(\rho^\xi + \rho^{\xi+N_s} \right)}} \left(\frac{1}{d} + \frac{\sqrt{\sum_{\xi=1,\xi\neq\beta}^{N_s} \left(\rho^\xi + \rho^{\xi+N_s} \right)}}{K} - 2y_c \left(\rho^\beta + \rho^{\beta+N_s} \right) \right). \tag{20}$$

Kinematic hardening is then introduced into the single crystal constitutive framework to describe the evolution of the backstress X^α at each individual slip system α. In this context, the backstress rate $\dot{X}^\alpha$ is modeled by the nonlinear Armstrong–Frederick law (Armstrong and Frederick, 1966), which depends on the slip rate $\dot{\gamma}^\alpha$ and the current backstress X^α as follows:

$$\forall \alpha = 1, \ldots, N_s : \dot{X}^\alpha = -\dot{X}^{\alpha+N_s} = C \operatorname{sgn}(\tau^\alpha) \left(\dot{\gamma}^\alpha + \dot{\gamma}^{\alpha+N_s} \right) - D(\dot{\gamma}^\alpha + \dot{\gamma}^{\alpha+N_s})X^\alpha, \tag{21}$$

where parameter C (resp. D) represents the direct hardening (resp. dynamic recovery) modulus and $\operatorname{sgn}(\tau^\alpha)$ denotes the sign of τ^α.

2.2. Numerical implementation

This section provides a brief description of the numerical implementation of the single crystal constitutive equations within the ABAQUS finite element code, using a User-defined MATerial subroutine (UMAT). In this implementation, an explicit integration scheme from the family of ultimate algorithms is used. It has been demonstrated in Akpama et al. (2016) that this integration scheme exhibits better robustness compared to the well-known return-mapping algorithm. In particular, it has been clearly shown in the latter study that adopting the ultimate algorithm can substantially reduce the computational cost by 1.5–5 times, as compared to the integration scheme based on the return-mapping algorithm, without compromising accuracy in numerical results. The main idea behind the ultimate algorithm is to decompose the finite element time increment $I^\Delta = [t_0, t_0 + \Delta t]$ into several sub-increments $I^{\delta_n} = [t_n, t_{n+1}]$, where the length of each sub-increment $\delta t_n = t_{n+1} - t_n$ is a priori unknown and should be computed in such a way that the Schmid condition remains satisfied for all the slip systems over I^{δ_n}. Under this approach, the single crystal constitutive equations are integrated over each sub-increment I^{δ_n}, and the different variables are updated from one sub-increment to the next. To emphasize the time dependency of the different quantities in the subsequent computational developments, a variable $\bullet$ evaluated at time t_n (resp. t_{n+1}) is denoted by $\bullet(t_n)$ (resp. $\bullet(t_{n+1})$).

One of the main inputs of the UMAT is the deformation gradient $\mathbf{f}(t_0)$ at the beginning of the time increment I^Δ, and its counterpart $\mathbf{f}(t_0 + \Delta t)$ at the end of I^Δ. The microscopic velocity gradient $\mathbf{g} = \dot{\mathbf{f}} \cdot \mathbf{f}^{-1}$ remains constant over I^Δ and, therefore, over each time sub-increment I^{δ_n}. It is obtained from $\mathbf{f}(t_0)$ and $\mathbf{f}(t_0 + \Delta t)$ using the following approximation:

$$\mathbf{g} = \left(\frac{\mathbf{f}(t_0 + \Delta t) - \mathbf{f}(t_0)}{\Delta t} \right) \cdot \left(\frac{\mathbf{f}(t_0 + \Delta t) + \mathbf{f}(t_0)}{2} \right)^{-1}. \tag{22}$$

In addition to the velocity gradient **g** determined by Eq. (22), we assume that the microscopic variables (namely, $\bar{\mathbf{r}}$, σ, γ^α, τ_c^α, ρ^α, and X^α for $\alpha = 1, \ldots, 2N_s$) are known at the beginning of the sub-increment I^{δ_n} (i.e., at t_n). These same variables should be updated at the end of I^{δ_n}, and the consistent tangent modulus $\mathbf{c}^{ep}$ required for the finite element computations, as well as for the bifurcation analysis, needs also to be determined. A careful examination of the constitutive equations reveals that the determination of the slip rates $\dot{\gamma}^\alpha(t_n)$ is sufficient to fully compute the values of the unknown variables at t_{n+1}. To compute these slip rates, we introduce the set of potentially active slip systems $\mathcal{P}$, which is defined as:

$$\mathcal{P} = \left\{ \alpha = 1, \ldots, 2N_s \ : \ \left(\tau^\alpha(t_n) - X^\alpha(t_n) \right) - \tau_c^\alpha(t_n) = 0 \right\}. \tag{23}$$

Once the set $\mathcal{P}$ is identified from Eq. (23), the Schmid law given in Eq. (13) can be restricted to systems belonging to $\mathcal{P}$ and formulated in its rate form as:

$$\forall \alpha \in \mathcal{P} \ : \ \dot{f}^\alpha(t_n) = \dot{\tau}_c^\alpha(t_n) - \left(\dot{\tau}^\alpha(t_n) - \dot{X}^\alpha(t_n) \right) \geq 0; \quad \dot{\gamma}^\alpha(t_n) \geq 0; \quad \dot{f}^\alpha(t_n) \dot{\gamma}^\alpha(t_n) = 0. \tag{24}$$

Using Eqs. (10), (11), (12), (15), (20) and (21), $\dot{f}^\alpha(t_n)$ in Eq. (24) can be mathematically expressed through the following developments:

$$\forall \alpha \in \mathcal{P} \ : \ \dot{f}^\alpha(t_n) = \dot{\tau}_c^\alpha(t_n) - \left(\dot{\tau}^\alpha(t_n) - \dot{X}^\alpha(t_n) \right) = \sum_{\beta \in \mathcal{P}} H^{\alpha\beta}(t_n) \dot{\gamma}^\beta(t_n) - \left(\dot{\bar{\sigma}}(t_n) : \mathbf{R}_0^\alpha - \dot{X}^\alpha(t_n) \right);$$

$$= \sum_{\beta \in \mathcal{P}} H^{\alpha\beta}(t_n) \dot{\gamma}^\beta(t_n) - \bar{\mathbf{d}}^e(t_n) : \bar{\mathbf{c}}^e : \mathbf{R}_0^\alpha + \dot{X}^\alpha(t_n);$$

$$= \sum_{\beta \in \mathcal{P}} H^{\alpha\beta}(t_n) \dot{\gamma}^\beta(t_n) - \left(\bar{\mathbf{d}}(t_n) - \sum_{\beta \in \mathcal{P}} \dot{\gamma}^\beta(t_n) \mathbf{R}_0^\beta \right) : \bar{\mathbf{c}}^e : \mathbf{R}_0^\alpha + \dot{X}^\alpha(t_n);$$

$$= \sum_{\beta \in \mathcal{P}} H^{\alpha\beta}(t_n) \dot{\gamma}^\beta(t_n) + \sum_{\beta \in \mathcal{P}} \left(\mathbf{R}_0^\alpha : \bar{\mathbf{c}}^e : \mathbf{R}_0^\beta \right) \dot{\gamma}^\beta(t_n) + \sum_{\beta \in \mathcal{P}} \delta^{\alpha\beta} \left(\mathrm{sgn}(\tau^\beta) C - D X^\beta(t_n) \right) \dot{\gamma}^\beta(t_n) - \mathbf{R}_0^\alpha : \bar{\mathbf{c}}^e : \bar{\mathbf{d}}(t_n);$$

$$\hat{=} \sum_{\beta \in \mathcal{P}} A^{\alpha\beta}(t_n) \dot{\gamma}^\beta(t_n) - B^\alpha(t_n), \tag{25}$$

where $\delta^{\alpha\beta}$ represents the Kronecker delta. Matrix $\mathbf{A}(t_n)$ and vector $\mathbf{B}(t_n)$ can easily be written in the following index forms:

$$\forall \alpha, \beta \in \mathcal{P} \ : \ \begin{cases} A^{\alpha\beta}(t_n) = H^{\alpha\beta}(t_n) + \left(\mathbf{R}_0^\alpha : \bar{\mathbf{c}}^e : \mathbf{R}_0^\beta \right) + \delta^{\alpha\beta} \left(\mathrm{sgn}(\tau^\beta) C - D X^\beta(t_n) \right); \\ B^\alpha(t_n) = \mathbf{R}_0^\alpha : \bar{\mathbf{c}}^e : \bar{\mathbf{d}}(t_n). \end{cases} \tag{26}$$

Using Eqs. (25) and (26), the rate form of the Schmid condition, as defined by Eq. (24), can be reformulated in the following general matrix form:

$$\forall \alpha \in \mathcal{P} \ : \ \begin{cases} \dot{f}^\alpha(t_n) = \sum_{\beta \in \mathcal{P}} A^{\alpha\beta}(t_n) \dot{\gamma}^\beta(t_n) - B^\alpha(t_n) \geq 0, \\ \dot{\gamma}^\alpha(t_n) \geq 0, \\ \left(\sum_{\beta \in \mathcal{P}} A^{\alpha\beta}(t_n) \dot{\gamma}^\beta(t_n) - B^\alpha(t_n) \right) \dot{\gamma}^\alpha(t_n) = 0. \end{cases} \tag{27}$$

It is important to note that the nonlinear complementarity problem (NLCP) defined by Eq. (16) is converted into a linear complementarity problem (LCP) when an explicit scheme is adopted to integrate the single crystal constitutive equations. In this explicit scheme, the components of matrix $\mathbf{A}$ and vector $\mathbf{B}$ remain constant over I^{δ_n} and are equal to their values at t_n. As a result, the set of active slip systems $\mathcal{A}$ ($\mathcal{A} \subset \mathcal{P}$ with $\dot{\gamma}^\alpha(t_n) > 0$ for all the slip systems α belonging to set $\mathcal{A}$) can be efficiently determined from the LCP using a combinatorial search procedure, similar to the one used in Ben Bettaieb et al. (2012). Furthermore, the slip rate $\dot{\gamma}^\alpha(t_n)$ of each active slip system α can be determined using the following equation:

$$\forall \alpha \in \mathcal{A} \ : \ \dot{\gamma}^\alpha(t_n) = \sum_{\beta \in \mathcal{A}} \Lambda^{\alpha\beta}(t_n) B^\beta(t_n) = \sum_{\beta \in \mathcal{A}} \Lambda^{\alpha\beta} \left(\mathbf{R}_0^\beta : \bar{\mathbf{c}}^e : \bar{\mathbf{d}}(t_n) \right), \tag{28}$$

where matrix $\Lambda(t_n)$ is the inverse of matrix $\mathbf{A}(t_n)$. The slip rates of the crystallographic slip systems belonging to $\mathcal{P} \setminus \mathcal{A}$ are obviously set to zero.

When the slip rates $\dot{\gamma}^\alpha(t_n)$ of the crystallographic systems belonging to set $\mathcal{P}$ are computed, the length of the current sub-increment δt_n ($\leq \Delta t$) can be determined to fulfill the Schmid criterion for all the slip systems over I^{δ_n}. As clearly shown in Eq. (27), this criterion is obviously satisfied for the potentially active slip systems ($\alpha \in \mathcal{P}$). Therefore, it needs to be verified for the other slip systems ($\alpha \notin \mathcal{P}$):

$$\forall \alpha \notin \mathcal{P} \ : \ \tau^\alpha(t_{n+1}) - X^\alpha(t_{n+1}) \leq \tau_c^\alpha(t_{n+1}), \tag{29}$$

where the expressions of τ^α and τ_c^α at time t_{n+1} can be explicitly updated by the following relations:

$$\forall \alpha \notin \mathcal{P} \ : \ \tau^\alpha(t_{n+1}) = \tau^\alpha(t_n) + \delta t_n \mathbf{R}_0^\alpha : \dot{\bar{\sigma}}(t_n) = \tau^\alpha(t_n) + \delta t_n \mathbf{R}_0^\alpha : \bar{\mathbf{c}}^e : \left(\bar{\mathbf{d}}(t_n) - \sum_{\beta \in \mathcal{P}} \dot{\gamma}^\beta(t_n) \mathbf{R}_0^\beta \right). \tag{30}$$

$$\forall \alpha \notin \mathcal{P} \ : \ \tau_c^\alpha(t_{n+1}) = \tau_c^{\alpha+N_s}(t_{n+1}) = \tau_c^\alpha(t_n) + \delta t_n \dot{\tau}_c^\alpha(t_n) = \tau_c^\alpha(t_n) + \delta t_n \sum_{\beta \in \mathcal{P}} H^{\alpha\beta}(t_n) \dot{\gamma}^\beta(t_n). \tag{31}$$

and $X^\alpha(t_{n+1})$ is equal to $X^\alpha(t_n)$ as slip system α is inactive ($\dot{\gamma}^\alpha(t_n) = 0$). Combination of Eqs. (29), (30), and (31) yields the following condition on the value of δt_n:

$$\delta t_n = min_{\alpha \notin P} \left\{ \Delta t, \ \frac{\tau_c^\alpha(t_n) - \left(\tau^\alpha(t_n) - X^\alpha(t_n)\right)}{\mathbf{R}_0^\alpha : \bar{\mathbf{c}}^e : \left(\bar{\mathbf{d}}(t_n) - \sum\limits_{\beta \in P} \dot{\gamma}^\beta(t_n)\mathbf{R}_0^\beta\right) - \sum\limits_{\beta \in P} H^{\alpha\beta}(t_n)\dot{\gamma}^\beta(t_n)} \right\}. \tag{32}$$

Once the length δt_n is computed from Eq. (32), the other mechanical variables could be updated at t_{n+1} as follows:

$$\begin{cases}
\delta\bar{\mathbf{r}}(t_n) = e^{\left(\delta t_n \left(\bar{w}(t_n) - \sum\limits_{\alpha \in A} \dot{\gamma}^\alpha(t_n)\mathbf{S}_0^\alpha\right)\right)}; \\
\bar{\mathbf{r}}(t_{n+1}) = \bar{\mathbf{r}}(t_n) \cdot \delta\bar{\mathbf{r}}(t_n); \\
\dot{\bar{\sigma}}(t_n) = \bar{\mathbf{c}}^e : \left(\bar{\mathbf{d}}(t_n) - \sum\limits_{\alpha \in A} \dot{\gamma}^\alpha(t_n)\mathbf{R}_0^\alpha\right); \\
\bar{\sigma}(t_{n+1}) = \bar{\sigma}(t_n) + \delta t_n \dot{\bar{\sigma}}(t_n); \\
\sigma(t_{n+1}) = \bar{\mathbf{r}}(t_{n+1}) \cdot \bar{\sigma}(t_{n+1}) \cdot \bar{\mathbf{r}}^T(t_{n+1}); \\
\forall \alpha = 1, \ldots, N_s : \dot{X}^\alpha(t_n) = -\dot{X}^{\alpha+N_s}(t_n) = C \, \text{sgn}(\tau^\alpha) \left(\dot{\gamma}^\alpha(t_n) + \dot{\gamma}^{\alpha+N_s}(t_n)\right) - D(\dot{\gamma}^\alpha(t_n) + \dot{\gamma}^{\alpha+N_s}(t_n))X^\alpha(t_n); \\
\forall \alpha = 1, \ldots, 2N_s : X^\alpha(t_{n+1}) = X^\alpha(t_n) + \delta t_n \dot{X}^\alpha(t_n); \\
\forall \alpha = 1, \ldots, 2N_s : \rho^\alpha(t_{n+1}) = \rho^\alpha(t_n) + \delta t_n \dot{\rho}^\alpha(t_n); \\
\forall \alpha = 1, \ldots, 2N_s : \gamma^\alpha(t_{n+1}) = \gamma^\alpha(t_n) + \delta t_n \dot{\gamma}^\alpha(t_n); \\
\forall \alpha = 1, \ldots, N_s : \tau_c^\alpha(t_{n+1}) = \tau_c^{\alpha+N_s}(t_{n+1}) = \tau_c^\alpha(t_n) + \delta t_n \sum\limits_{\beta \in A} H^{\alpha\beta}\dot{\gamma}^\beta(t_n).
\end{cases} \tag{33}$$

and the consistent tangent modulus $\bar{\mathbf{c}}^{ep}$ should be determined as follows:

$$\bar{\mathbf{c}}^{ep} = \frac{\partial \delta\bar{\sigma}}{\partial \delta\bar{\varepsilon}} = \bar{\mathbf{c}}^e - \sum_{\alpha \in A}\sum_{\beta \in A} \Lambda^{\alpha\beta}(t_n)\left(\bar{\mathbf{c}}^e : \mathbf{R}_0^\alpha + \mathbf{S}_0^\alpha \cdot \bar{\sigma}(t_n) - \bar{\sigma}(t_n) \cdot \mathbf{S}_0^\alpha\right) \otimes \left(\mathbf{R}_0^\beta : \bar{\mathbf{c}}^e\right). \tag{34}$$

The consistent tangent matrix defined in the current configuration $\mathbf{c}^{ep}$ can be obtained by rotating its counterpart $\bar{\mathbf{c}}^{ep}$ from the single crystal frame to the current frame. After updating all the mechanical variables and the consistent tangent modulus, the computation should proceed to the next new sub-increment I^{δ_n}.

2.3. Periodic homogenization scheme

In this study, we have chosen the periodic homogenization technique to estimate the macroscopic behavior of the unit cell based on the behavior of the individual constituent single crystals. Additionally, the macroscopic nominal stress rate tensor $\dot{\mathbf{N}}$ and the macroscopic velocity gradient $\mathbf{G}$ are selected as appropriate work-conjugate stress and strain measures. Similar to previous investigations, the macroscopic plane-stress assumption is considered to predict the FLDs. The in-plane part of a vector or tensor $\bullet$ is denoted $^{IN}\bullet$. To be concise, only the key equations and steps describing this technique are provided in what follows, while more comprehensive information can be found in Zhu et al. (2020b).

- The macroscopic velocity gradient $\mathbf{G}$ and the macroscopic nominal stress rate tensor $\dot{\mathbf{N}}$ are related to their corresponding microscopic counterparts $\mathbf{g}$ and $\dot{\mathbf{n}}$ through the following averaging relations:

$$\mathbf{G} = \frac{1}{|\mathcal{V}|}\int_\mathcal{V} \mathbf{g}\, d\mathcal{V} \quad \text{and} \quad \dot{\mathbf{N}} = \frac{1}{|\mathcal{V}|}\int_\mathcal{V} \dot{\mathbf{n}}\, d\mathcal{V}, \tag{35}$$

where $\mathcal{V}$ is the current volume of the unit cell.

- The microscopic static equilibrium equation is defined as follows:

$$div_\mathbf{x}(\dot{\mathbf{n}}^T) = \mathbf{0}, \tag{36}$$

where $\mathbf{x}$ represents the current coordinate of the material point.

- The current in-plane velocity $^{IN}\mathbf{v}$ is assumed to be linked to the current in-plane position $^{IN}\mathbf{x}$ and to the in-plane macroscopic velocity gradient $^{IN}\mathbf{G}$ as:

$$^{IN}\mathbf{v} = {}^{IN}\mathbf{G} \cdot {}^{IN}\mathbf{x} + {}^{IN}\mathbf{v}_{per}, \tag{37}$$

where $^{IN}\mathbf{v}_{per}$ is an in-plane periodic velocity fluctuation field.

- The application of the periodic homogenization technique by imposing the PBCs on the unit cell, as will be explained in Section 3.2.1.

2.4. Rice bifurcation criterion

The Rice bifurcation criterion (Rice, 1976) is employed to predict the incipience of macroscopic localized necking. This criterion detects the loss of ellipticity of the macroscopic constitutive equations, which is shown to be associated with a sudden jump in the strain rate across a localization band, as shown in Fig. 2. For brevity, only the main lines of the Rice bifurcation criterion are presented in this section. More detailed information about this criterion can be found in Ben Bettaieb and Abed-Meraim (2015). The occurrence of strain localization can be determined based on the following conditions:

The first condition: Maxwell's compatibility condition for the velocity fields, stating that there exists a jump vector $\dot{\vec{C}}$ such that the jump in $^{\text{IN}}\mathbf{G}$ reads:

$$[[^{\text{IN}}\mathbf{G}]] = {^{\text{IN}}\mathbf{G}^{\text{O}}} - {^{\text{IN}}\mathbf{G}^{\text{I}}} = \dot{\vec{C}} \otimes \vec{\mathcal{N}}. \tag{38}$$

where:

- $[[^{\text{IN}}\mathbf{G}]]$ denotes the jump in the in-plane velocity gradient field $^{\text{IN}}\mathbf{G}$ across the localization band.
- $^{\text{IN}}\mathbf{G}^{\text{O}}$ and $^{\text{IN}}\mathbf{G}^{\text{I}}$ are the in-plane velocity gradient outside and inside the band, respectively.
- $\vec{\mathcal{N}}$ represents the unit vector, which is normal to the localization band and defined by $(cos\theta, sin\theta)$ for $0 \leq \theta \leq \pi/2$.

The second condition: the stress equilibrium condition assuming the continuity of the macroscopic in-plane nominal stress rate tensor $^{\text{IN}}\dot{\mathbf{N}}$ across the localization band of normal unit vector $\vec{\mathcal{N}}$:

$$[[^{\text{IN}}\dot{\mathbf{N}}^T]] \cdot \vec{\mathcal{N}} = \vec{\mathbf{0}}. \tag{39}$$

The in-plane tensors $^{\text{IN}}\mathbf{G}$ and $^{\text{IN}}\dot{\mathbf{N}}$ are related through the following generic macroscopic constitutive law:

$$^{\text{IN}}\dot{\mathbf{N}} = {^{\text{IN}}\mathbf{L}} : {^{\text{IN}}\mathbf{G}}. \tag{40}$$

where $^{\text{IN}}\mathbf{L}$ is the in-plane macroscopic tangent modulus.

By substituting Eqs. (38), (40) into (39), the stress equilibrium equation can be rewritten as:

$$\vec{\mathcal{N}} \cdot \left[{^{\text{IN}}\mathbf{L}} : \left(\dot{\vec{C}} \otimes \vec{\mathcal{N}} \right) \right] = \vec{\mathbf{0}}. \tag{41}$$

which is equivalent to:

$$\left(\vec{\mathcal{N}} \cdot {^{\text{IN}}\mathbf{L}} \cdot \vec{\mathcal{N}} \right) \cdot \dot{\vec{C}} = \vec{\mathbf{0}}. \tag{42}$$

The second-order tensor $\vec{\mathcal{N}} \cdot {^{\text{IN}}\mathbf{L}} \cdot \vec{\mathcal{N}}$ introduced in Eq. (42) is the so-called in-plane acoustic tensor. As long as this tensor is invertible, the components of the jump vector $\dot{\vec{C}}$ are equal to zero and, consequently, the deformation remains homogeneous. However, when the in-plane acoustic tensor becomes singular, this implies that there is an infinite number of jump vectors that satisfy Eq. (42), thus indicating an effective bifurcation. The singularity of $\vec{\mathcal{N}} \cdot {^{\text{IN}}\mathbf{L}} \cdot \vec{\mathcal{N}}$ signifies the initiation of plastic strain localization:

$$\det \left(\vec{\mathcal{N}} \cdot {^{\text{IN}}\mathbf{L}} \cdot \vec{\mathcal{N}} \right) = 0. \tag{43}$$

To apply the Rice bifurcation criterion, the in-plane macroscopic tangent modulus $^{\text{IN}}\mathbf{L}$ should first be computed. The condensation technique, originally proposed by Miehe (2003), is adopted to determine this modulus from the global FE stiffness matrix. The basic algorithmic steps of this technique are summarized as follows:

- Add the ABAQUS keyword 'Element Matrix Output' in the '.inp' file to output the elementary stiffness matrices $\mathbf{K}_{el}$ for each FE computation time increment. These matrices are stored in a '.mtx' format file.
- Subdivide the entire node set into two subsets: one comprising nodes within the interior of the unit cell denoted as 'a', and the second comprising nodes located on the boundary of the unit cell referred to as 'b'.
- Assemble the global stiffness matrix $\mathbf{K}$ from the elementary matrices $\mathbf{K}_{el}$ using the connectivity of the different nodes.
- Partition the global stiffness matrix $\mathbf{K}$ into four sub-matrices $\mathbf{K}_{aa}$, $\mathbf{K}_{ab}$, $\mathbf{K}_{ba}$ and $\mathbf{K}_{bb}$ as follows:

$$\mathbf{K} = \begin{bmatrix} \mathbf{K}_{aa} & \mathbf{K}_{ab} \\ \mathbf{K}_{ba} & \mathbf{K}_{bb} \end{bmatrix}. \tag{44}$$

- Construct the projection matrices $\mathbb{Q}$ and $\mathbb{H}$ defined in Zhu et al. (2022).
- Compute the macroscopic tangent modulus $\mathbf{C}$, which relates the macroscopic first Piola–Kirchhoff stress rate tensor $\dot{\mathbf{P}}$ to the macroscopic deformation gradient rate $\dot{\mathbf{F}}$ in their 3D forms ($\dot{\mathbf{P}} = \mathbf{C}:\dot{\mathbf{F}}$), through the following relation:

$$\mathbf{C} = \frac{1}{|\mathcal{V}_0|} \mathbb{Q} \cdot \left[\mathbb{H} \cdot \left(\mathbf{K}_{bb} - \mathbf{K}_{ba} \cdot \mathbf{K}_{aa}^{-1} \cdot \mathbf{K}_{ab} \right) \cdot \mathbb{H}^T \right]^{-1} \cdot \mathbb{Q}^T, \tag{45}$$

where $\mathcal{V}_0$ is the initial volume of the unit cell.

- Determine the index form of the in-plane macroscopic tangent modulus $^{\text{IN}}\mathbf{C}$ by the following condensation procedure:

$$\forall i, j, k, l = 1, 2 : {^{\text{IN}}C_{ijkl}} = C_{ijkl} - \frac{C_{ij33}C_{33kl}}{C_{3333}}. \tag{46}$$
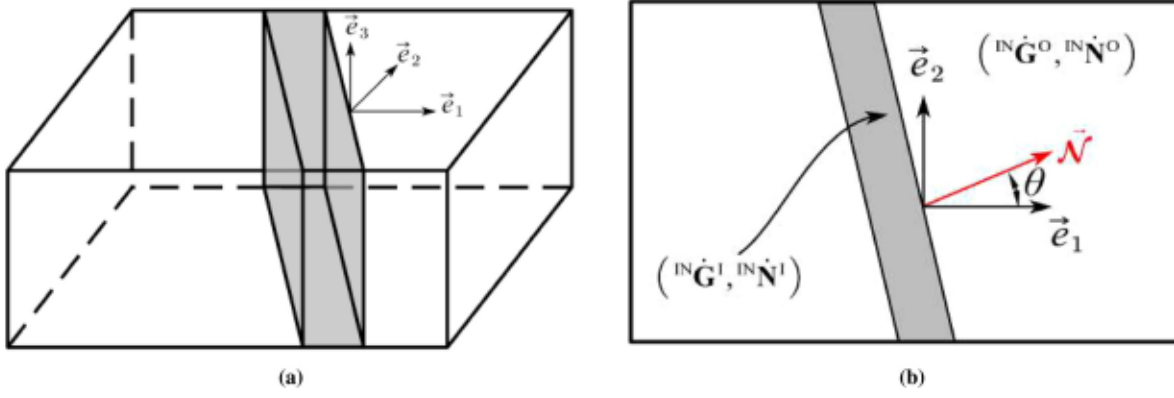
Fig. 2. Illustration of the Rice bifurcation criterion: (a) presentation of the unit cell with the localization band; (b) 2D presentation.

- Derive the in-plane macroscopic tangent modulus $^{IN}\mathbf{L}$, which links the in-plane macroscopic nominal stress rate $^{IN}\dot{\mathbf{N}}$ ($=^{IN}\dot{\mathbf{P}}^T$) to the in-plane macroscopic velocity gradient $^{IN}\mathbf{G}$, from the in-plane macroscopic tangent modulus $^{IN}\mathbf{C}$ by permutation of the first two indices as follows:

$$\forall i,j,k,l = 1,2 : {}^{IN}L_{ijkl} = {}^{IN}C_{jikl}. \tag{47}$$

- Compute the components of the second-order in-plane acoustic tensor $\vec{\mathcal{N}} \cdot {}^{IN}\mathbf{L} \cdot \vec{\mathcal{N}}$, introduced in Eq. (43), by the following relation:

$$\forall i,j,k,l = 1,2 : \left(\vec{\mathcal{N}} \cdot {}^{IN}\mathbf{L} \cdot \vec{\mathcal{N}}\right)_{jk} = \sum_{i=1}^{2} \sum_{l=1}^{2} \mathcal{N}_i \cdot {}^{IN}L_{ijkl} \cdot \mathcal{N}_l, \text{ where } \mathcal{N}_1 = cos\theta \text{ and } \mathcal{N}_2 = sin\theta. \tag{48}$$

More practical details about these condensation techniques and their implementation in a set of Python codes can be found in Zhu et al. (2022). Localized necking occurs when the minimum value of the in-plane acoustic tensor Min $\left[\det\left(\vec{\mathcal{N}} \cdot {}^{IN}\mathbf{L} \cdot \vec{\mathcal{N}}\right)\right]$ over all possible band orientations θ ($0 \leq \theta \leq \pi/2$) vanishes for the first time. The same procedure is repeated for each strain-path ratio ρ ($-0.5 \leq \rho \leq 1$), with $\Delta\rho = 0.1$, to obtain the complete FLD (Akpama et al., 2017).

3. Results and discussions

3.1. Material parameter determination and numerical implementation validation

3.1.1. Finite element model

This section aims to validate the implementation of the selected hardening model. To achieve this, a thin metal sheet with a spatially periodic structure is chosen, and a Representative Volume Element (RVE), also known as a unit cell, is identified to accurately represent this sheet. The unit cell should encapsulate essential microscopic features and effectively capture the homogenized properties of the bulk medium. Previous contributions (Haouala et al. 2018, Luo et al. 2013 among others) have shown that an RVE containing a minimum of 200 FCC grains with random shapes is suitable for this purpose. This conclusion is confirmed by the results of the grain number sensitivity study presented in Appendix B. Therefore, a unit cell consisting of 200 grains is generated by the NEPER software, and the Voronoi tessellation technique (Quey et al., 2011) is used to define the grain shape and arrangement (Fig. 3(a)). The initial size of the generated RVE is set to 1 mm × 1 mm × 1 mm. The corresponding grain size distribution is plotted in Fig. 3(b), with an average grain size of approximately 0.173289 mm (obtained from the NEPER software output). The unit cell generated by the NEPER software is meshed by 16 × 16 × 16 finite elements using the GMSH software (Geuzaine and Remacle, 2009), and it is subsequently converted into an ABAQUS input file. To generate this mesh, the finite element C3D20 (20-node quadratic hexahedral element with full integration) is used. The initial crystallographic texture is assumed to follow a random distribution and is designed by the ATEX software (Beausir and Fundenberger, 2017). Fig. 3(c) displays the (111) pole figure of the generated random crystallographic texture, with the rolling and transverse directions aligned with the X and Y directions, respectively. A Python script is developed to assign the crystallographic orientations to the different integration points of the finite element model.

3.1.2. Determination of the microscopic material parameters

In the current section, we will briefly outline the procedure for determining the microscopic material parameters for the various hardening models, which can be grouped into three categories: elasticity, dislocation density-based isotropic hardening, and kinematic hardening parameters. Table 1 provides a list of the identified material parameters, where most of the mixed hardening parameters were collected from several sources, including Harder (1999), Yoshida and Kuroda (2012), Bratov and Borodin (2015),
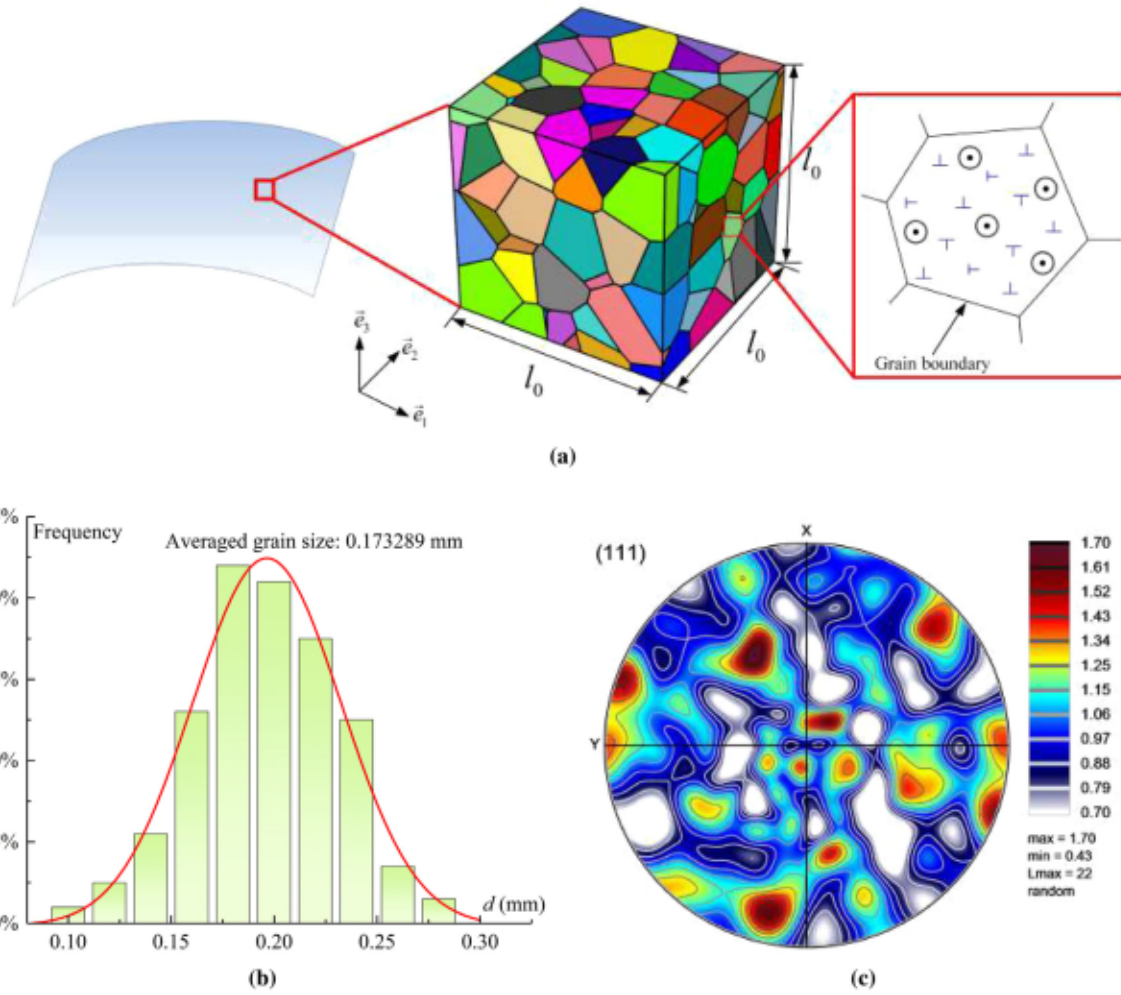
Fig. 3. (a) Morphological description of the unit cell containing 200 randomly shaped grains; (b) grain size distribution within the unit cell; (c) (111) pole figure corresponding to the initial random texture.

Table 1
Summary of the material parameters for various hardening models.

	Mixed hardening	Source	Isotropic hardening
Elasticity	$E = 65$ GPa, $v = 0.3$	Yoshida and Kuroda (2012)	$E = 65$ GPa, $v = 0.3$
	$\mu = 25$ GPa	$\mu = E/2(1+v)$	$\mu = 25$ GPa
Dislocation density-based hardening	$\tau_0 = 50$ MPa		$\tau_0 = 50$ MPa
	$b = 2.86 \times 10^{-7}$ mm	Bratov and Borodin (2015)	$b = 2.86 \times 10^{-7}$ mm
	$A = 0.35$	Yoshida (2022)	$A = 0.4$
	$\rho_0 = 1 \times 10^8$ mm^{-2}	Banerjee and Bhawalkar (2008)	$\rho_0 = 1 \times 10^8$ mm^{-2}
	$d = 0.173289$ mm	NEPER	$d = 0.173289$ mm
	$y_c = 10b$	Meng (2020)	$y_c = 9.85b$
	$K = 10$		$K = 7.4$
Kinematic hardening	$C = 200$ MPa		–
	$D = 3.5$	Harder (1999)	–

Lu et al. (2016), Meng (2020), Yoshida (2022). The macroscopic equivalent von Mises stress–strain response obtained from the simulation of a uniaxial tension test using the identified mixed hardening parameters is shown in Fig. 4 (the black curve). To ensure that the material parameters for the isotropic hardening model yield a mechanical response that is similar to the mixed hardening model, we have identified and adjusted the parameters accordingly. The best-fitting and calibrated material parameters for the isotropic hardening model are also reported in Table 1. The data provided in Fig. 4 illustrate this calibration process and show how the isotropic hardening model can closely replicate the mechanical behavior of the mixed hardening model.
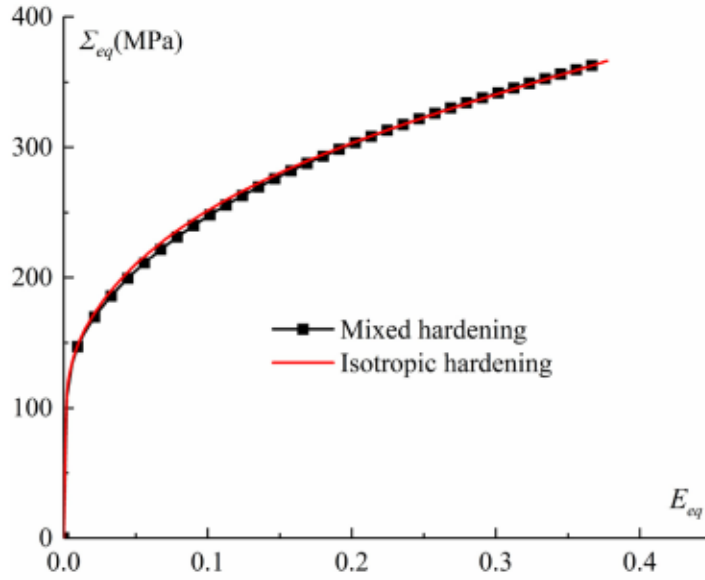
Fig. 4. Identification of the isotropic hardening parameters by numerical simulations of uniaxial tension test.

3.1.3. Mechanical response under cyclic loading

The boundary conditions and loading history, as presented in Fig. 5, are applied to simulate the mechanical behavior of a unit cell subjected to cyclic loading. The hysteresis loop, obtained through simulations of a complete cyclic loading, is depicted in Fig. 6(a). In these simulations, both isotropic and mixed hardening models are used for comparison. Additionally, the macroscopic stress–strain responses of the isotropic hardening model under uniaxial tension and compression are included in Fig. 6(a). It is noteworthy that the use of isotropic hardening model results in gradual increase in yield stresses at the onset of plastic deformation across various loading stages, as indicated by the comparison between the blue and black data points in Fig. 6(a). In contrast, the mixed hardening model predicts an initial rise in yield stress, which subsequently stabilizes during the final loading stage spanning from $0.75\,\text{s}$ to $1.0\,\text{s}$, as demonstrated in Fig. 6(a). This stabilization occurs because a dynamic equilibrium is reached between dislocation generation and annihilation, establishing a steady state that maintains stress at an approximately constant level. Moreover, the mixed hardening model exhibits nearly identical yield stresses at the onset of plastic deformation under tension or compression, both of which are lower than the yield stress predicted by the isotropic hardening model. As expected, the mixed hardening model demonstrates a pronounced Bauschinger effect. To quantitatively assess this effect, we compute the Bauschinger coefficient B_β as defined according to Lin et al. (2020) and Hou et al. (2022). The computed value of B_β is 0.3032, confirming the presence of this effect, primarily attributable to the backstress evolution and dislocation motion (Fig. 6(b)). The numerical predictions presented in Fig. 6 highlight the capability of the hardening model to accurately capture the single crystal plasticity hardening behavior.

The effect of the hardening model on the evolution of crystallographic texture during cyclic loading is analyzed by comparing the (111) pole figures presented in Fig. 7. In these figures, crystallographic textures are plotted at the end of each loading stage. A quick comparison between the initial texture presented in Fig. 3(c) and the textures shown in Fig. 7 reveals that the deformed textures exhibit higher magnitudes and more distinct features compared to the initial texture. This difference is particularly pronounced after the tension loading and reverse loading stages, indicating that the grains undergo significant rotation and large deformation. However, the texture observed after unloading deformation closely resembles the initial texture. Moreover, it is evident that the simulated texture is very similar for the different hardening models under cyclic loading. Nevertheless, the deformed texture is slightly more pronounced in the case of isotropic hardening. This observation aligns well with the conclusions drawn by Brahme et al. (2011), who demonstrated that considering the backstress effect leads to a reduction in crystallographic rotation during cyclic loading.

3.2. FLD predictions

3.2.1. Finite element model and macroscopic boundary conditions

The unit cell described in Section 3.1.1 is subjected to biaxial stretching along the $\vec{e}_1$ and $\vec{e}_2$ directions, as illustrated in Fig. 8. This loading configuration is adopted for the prediction of the ductility limits and their representation in the form of FLDs. Moreover, the out-of-plane components of the macroscopic nominal stress rate $\dot{\mathbf{N}}$: $\dot{N}_{13}$, $\dot{N}_{23}$, $\dot{N}_{31}$, $\dot{N}_{32}$, and $\dot{N}_{33}$ are held at zero. The strain-path ratio $\rho = G_{22}/G_{11}$ is maintained constant during the loading history, ranging from -0.5 (uniaxial tension state) to 1 (equibiaxial
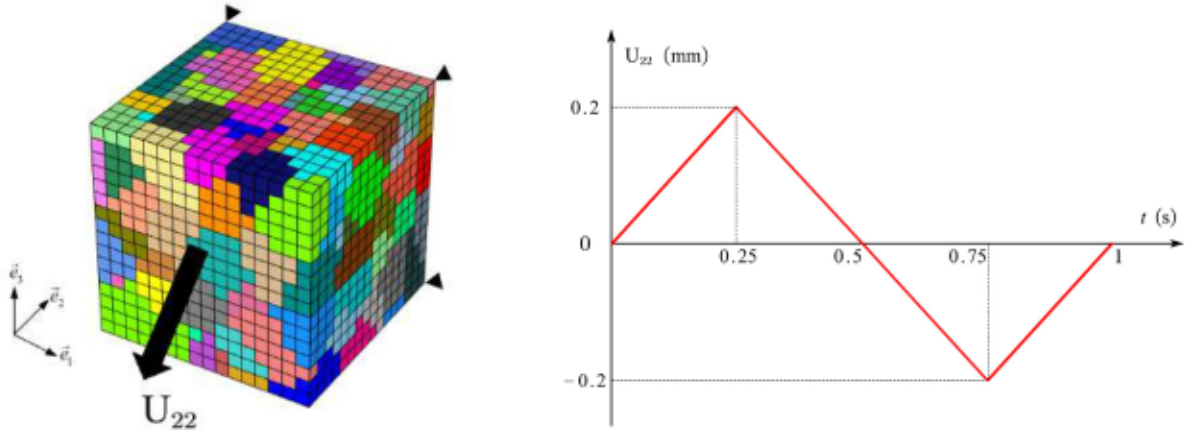
Fig. 5. Boundary conditions and loading history for unit cell simulations under cyclic loading.
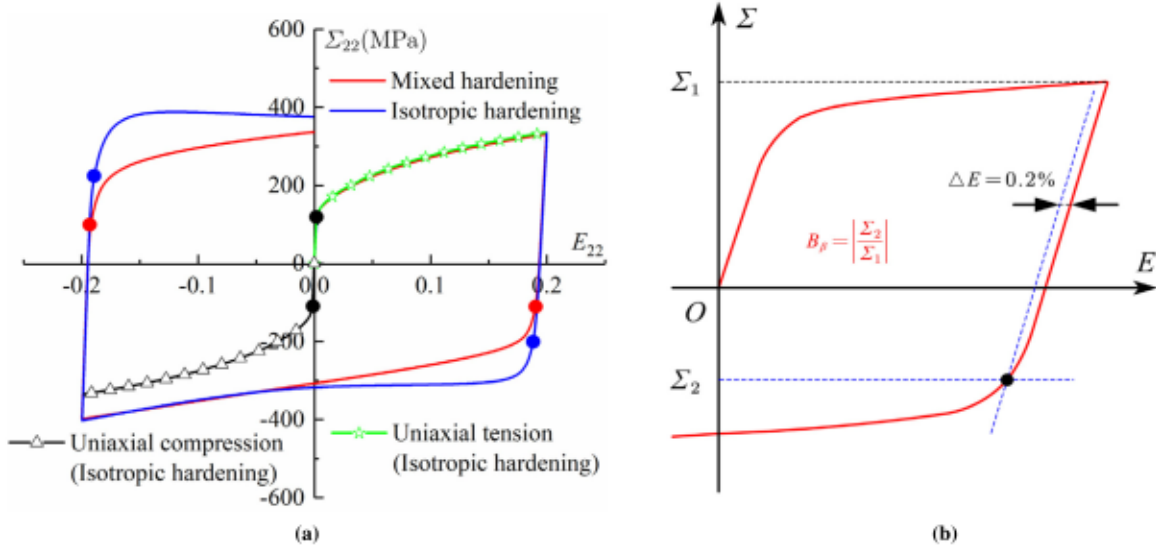

(a)
(b)

Fig. 6. (a) Cyclic stress–strain responses obtained with isotropic and mixed hardening models; (b) schematic definition of the Bauschinger coefficient B_β.

tension state). Also, in this loading configuration, the other in-plane components of the macroscopic velocity gradient $\mathbf{G}$ (i.e., G_{12} and G_{21}) are set to zero. The PBCs are only enforced on the faces $S_{01}^- : x_{01} = -\frac{l_0}{2}; S_{01}^+ : x_{01} = \frac{l_0}{2}, S_{02}^- : x_{02} = -\frac{l_0}{2}; S_{02}^+ : x_{02} = \frac{l_0}{2}$ (see Fig. 8). However, the two faces in direction $\vec{e}_3$ are left unconstrained. The latter condition allows the macroscopic plane-stress assumption to be ensured. For each strain path, the macroscopic tensors $\mathbf{G}$ and $\dot{\mathbf{N}}$ have the following generic forms:

$$\mathbf{G} = \begin{pmatrix} G_{11} & 0 & \divideontimes \\ 0 & \rho\, G_{11} & \divideontimes \\ \divideontimes & \divideontimes & \divideontimes \end{pmatrix}; \quad \dot{\mathbf{N}} = \begin{pmatrix} \divideontimes & \divideontimes & 0 \\ \divideontimes & \divideontimes & 0 \\ 0 & 0 & 0 \end{pmatrix}, \tag{49}$$

where '$\divideontimes$' indicates an unknown component, which should be determined by finite element simulations. The out-of-plane components $G_{13}, G_{31}, G_{23}, G_{32}$ and G_{33} of tensor $\mathbf{G}$ can be determined using the plane-stress conditions:

$$\dot{N}_{13} = \dot{N}_{31} = \dot{N}_{23} = \dot{N}_{32} = \dot{N}_{33} = 0. \tag{50}$$

The macroscopic loading defined by Eq. (49) can be expressed in a Lagrangian formulation, which is more suitable for the application of the HOMTOOLS:

$$\mathbf{F} = \begin{pmatrix} F_{11} & 0 & \divideontimes \\ 0 & (F_{11})^\rho & \divideontimes \\ \divideontimes & \divideontimes & \divideontimes \end{pmatrix}; \quad \mathbf{P} = \begin{pmatrix} \divideontimes & \divideontimes & 0 \\ \divideontimes & \divideontimes & 0 \\ 0 & 0 & 0 \end{pmatrix}, \tag{51}$$
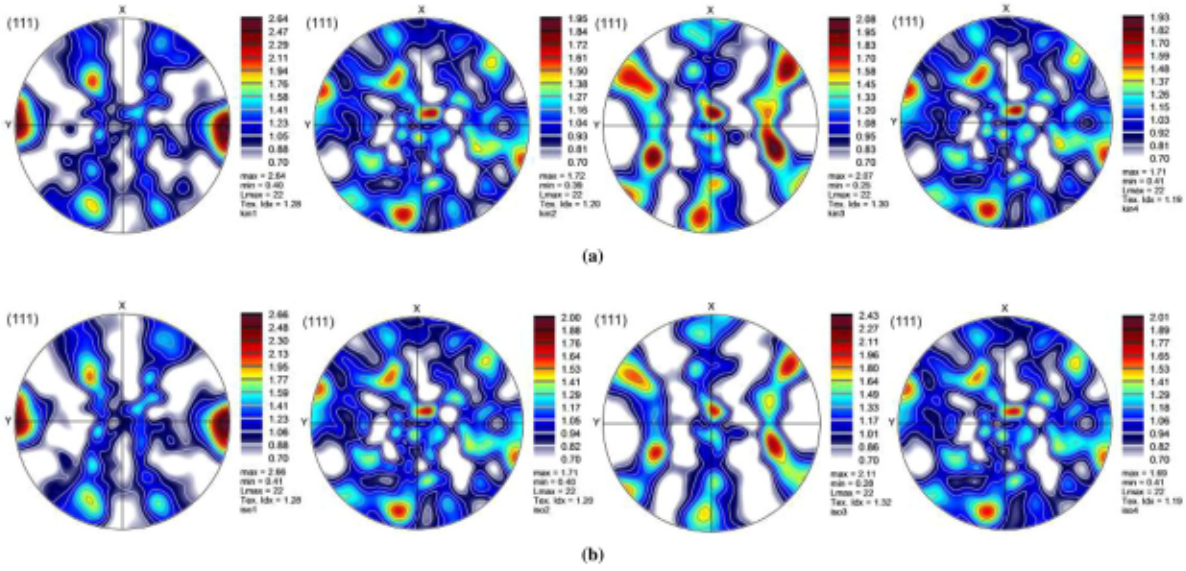
Fig. 7. Effect of the hardening model on the texture evolution at times $t = 0.25, 0.5, 0.75,$ and 1 s (corresponding to the end of each loading stage) for: (a) mixed hardening; (b) isotropic hardening.
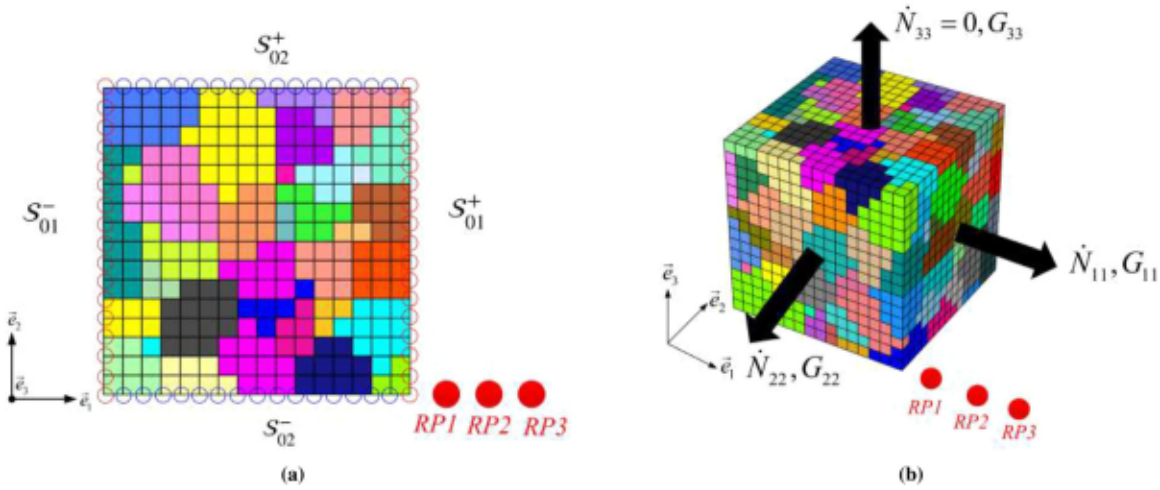

Fig. 8. (a) PBCs applied on the surfaces $S_{01}^-, S_{01}^+, S_{02}^-$ and S_{02}^+ of the unit cell (2D plane); (b) finite element mesh and the applied macroscopic loading to predict the FLDs.

where $\mathbf{F}$ is the macroscopic deformation gradient and $\mathbf{P}$ represents the macroscopic first Piola–Kirchhoff stress tensor ($\mathbf{P} = \mathbf{N}^T$). To apply the in-plane periodic boundary conditions and the macroscopic loading given by Eq. (51), three reference points $RP1$, $RP2$ and $RP3$ are created. The following prescribed boundary conditions should be applied to these reference points:

$$\begin{cases} RP1 : U_{11} = (F_{11} - 1)l_0; U_{12} = 0; U_{13} = 0, \\ RP2 : U_{21} = 0; U_{22} = ((F_{11})^\rho - 1)l_0; U_{23} = 0, \\ RP3 : RF_{31} = 0; RF_{32} = 0; RF_{33} = 0. \end{cases} \tag{52}$$

3.2.2. Bifurcation analysis

As discussed in Section 2.4, the in-plane macroscopic tangent modulus $^{IN}\mathbf{L}$ plays a crucial role in determining the ductility limits using the Rice bifurcation criterion. Therefore, the evolution of the components $^{IN}L_{1111}$ and $^{IN}L_{1212}$ is investigated and discussed in this section. Fig. 9 provides the evolution of these components ($^{IN}L_{1111}$ and $^{IN}L_{1212}$) in terms of the macroscopic strain component $E_{11} = \int_0^t G_{11} dt$ for the following strain-path ratios: $\rho = -0.5$ (uniaxial tensile state), $\rho = 0$ (plane strain tensile state), and $\rho = 1$ (equibiaxial tensile state). Both of the mixed and isotropic hardening models are considered to achieve these predictions. The
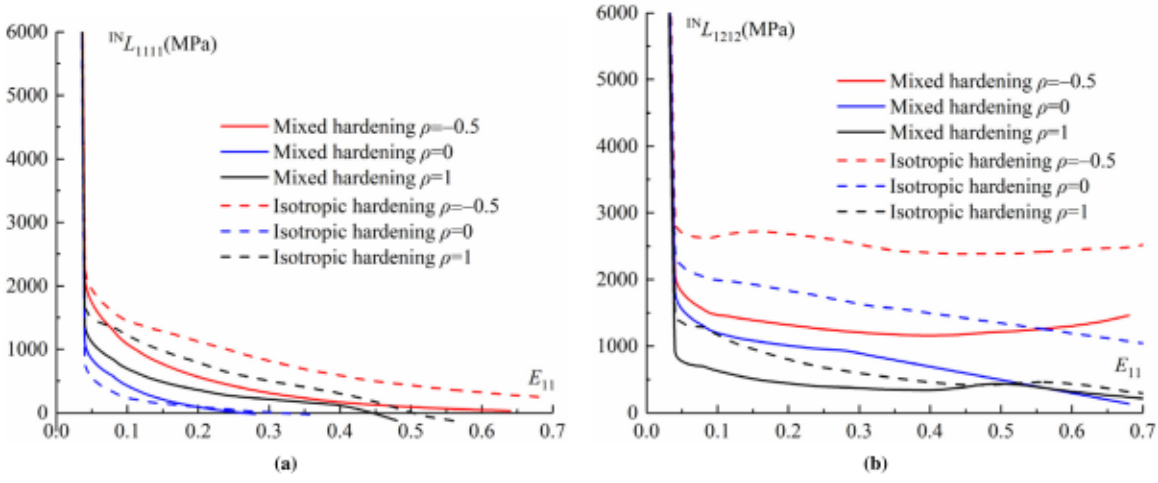
Fig. 9. Evolution of the components $^{IN}L_{1111}$ and $^{IN}L_{1212}$ of the in-plane macroscopic tangent modulus $^{IN}\mathbf{L}$ as functions of E_{11} for the three strain-path ratios $\rho = -0.5$, $\rho = 0$, and $\rho = 1$ for mixed and isotropic hardening models.

simulation results show that the component $^{IN}L_{1111}$ decreases rapidly and its value becomes very low (even negative in some cases). Similarly, the shearing component $^{IN}L_{1212}$ is also reduced after the elastic deformation stage. This phenomenon arises as an inherent consequence of the multi-slip character of crystal plasticity, leading to the formation of vertices on the single crystal yield surface. It is noteworthy that such a reduction in this shearing component presents the primary destabilizing factor leading to bifurcation and consequently promoting plastic strain localization. It should be highlighted that when a smooth yield surface with rounded corners is used, the component $^{IN}L_{1212}$ remains almost unchanged from its elastic value during plastic deformation, as shown in several studies such as Yoshida et al. (2009) and Akpama et al. (2016). In such a situation, strain localization cannot be predicted without the introduction of an initial geometric imperfection (Marciniak and Kuczyński, 1967). Furthermore, Fig. 9 reveals that the components $^{IN}L_{1111}$ and $^{IN}L_{1212}$ corresponding to the mixed hardening model are consistently lower than their counterparts obtained by the isotropic hardening model for the three strain paths. Hence, the ductility limits predicted by the mixed hardening model would also be lower than those determined by the isotropic hardening model.

To further illustrate the application of the bifurcation theory in detecting the onset of plastic strain localization, special attention is given to the evolution of the cubic root of the minimum determinant of the macroscopic acoustic tensor $\vec{\mathcal{N}} \cdot {}^{IN}\mathbf{L} \cdot \vec{\mathcal{N}}$, denoted as $\mathrm{Min}\left[\det\left(\vec{\mathcal{N}} \cdot {}^{IN}\mathbf{L} \cdot \vec{\mathcal{N}}\right)\right]^{1/3}$, for the three specific strain-path ratios $\rho = -0.5$, $\rho = 0$, and $\rho = 1$. The evolution of $\mathrm{Min}\left[\det\left(\vec{\mathcal{N}} \cdot {}^{IN}\mathbf{L} \cdot \vec{\mathcal{N}}\right)\right]^{1/3}$ is plotted in terms of the macroscopic strain component E_{11} in Fig. 10. It is important to note that the different curves are plotted until the initiation of strain localization, indicated by different symbols in Fig. 10. The analysis of the effect of the selected hardening model on these evolution curves reveals a significant reduction in ductility limits when kinematic hardening is considered. A more comprehensive investigation of the impact of kinematic hardening will be conducted in Section 3.2.6.

3.2.3. Effect of the initial dislocation density ρ_0

The initial dislocation density ρ_0 is an important microstructural parameter that can exert a substantial influence on the evolution of the CRSS as described in Eq. (17). Consequently, it affects the mechanical behavior and ductility limits. In this section, numerical simulations using the mixed hardening model are carried out to study the effect of the initial dislocation density ρ_0 on the ductility limits. To this end, three different values of ρ_0 are used: 1×10^8 mm^{-2}, 2×10^8 mm^{-2}, and 4×10^8 mm^{-2}. The results demonstrate that the value of ρ_0 has an important effect on the predicted ductility limits. As expected, the ductility limits decrease as the value of ρ_0 increases, as shown in Fig. 11(a). This finding is also supported by the evolution of the macroscopic equivalent von Mises stress Σ_{eq} versus the macroscopic equivalent strain E_{eq} for the uniaxial tensile state ($\rho = -0.5$), as depicted in Fig. 11(b). This result implies that the work-hardening behavior would decrease when the initial dislocation density increases. This observation, which is a direct consequence of dislocation annihilation, is very consistent with that reported in Lu et al. (2022). It must be pointed out that in real materials, the initial dislocation density can vary significantly from the different slip systems. However, for the sake of simplicity in this study, we have assumed that ρ_0 has the same value for all the slip systems.

3.2.4. Effect of the critical annihilation distance of dislocations y_c

Dislocations can be annihilated through various processes, such as dislocation intersection, mutual annihilation with opposite signs, or annihilation at obstacles or grain boundaries. The parameter y_c introduced in Eq. (19) controls the annihilation capability and induces strain softening during plastic deformation. To explore the impact of this parameter on the ductility limits, FLD simulations are performed with three different critical annihilation distances: $y_c = 5\,b$, $y_c = 10\,b$, and $y_c = 20\,b$ (with b the magnitude
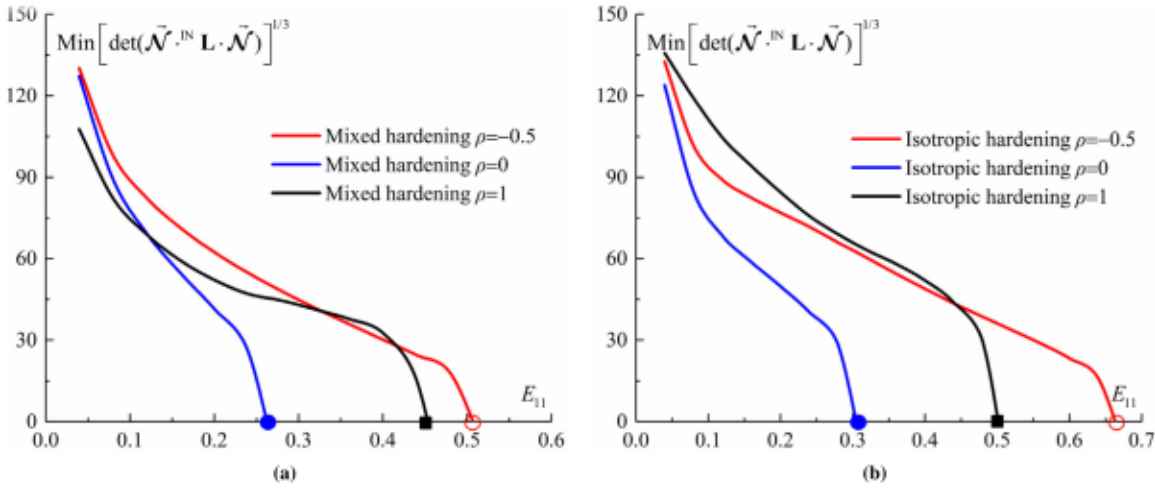
Fig. 10. Evolution of the cubic root of the minimum of the determinant of the macroscopic acoustic tensor $\vec{\mathcal{N}} \cdot {}^{IN}\mathbf{L} \cdot \vec{\mathcal{N}}$ versus the macroscopic strain component E_{11} for the three strain-path ratios $\rho = -0.5$, $\rho = 0$, and $\rho = 1$: (a) mixed hardening; (b) isotropic hardening.
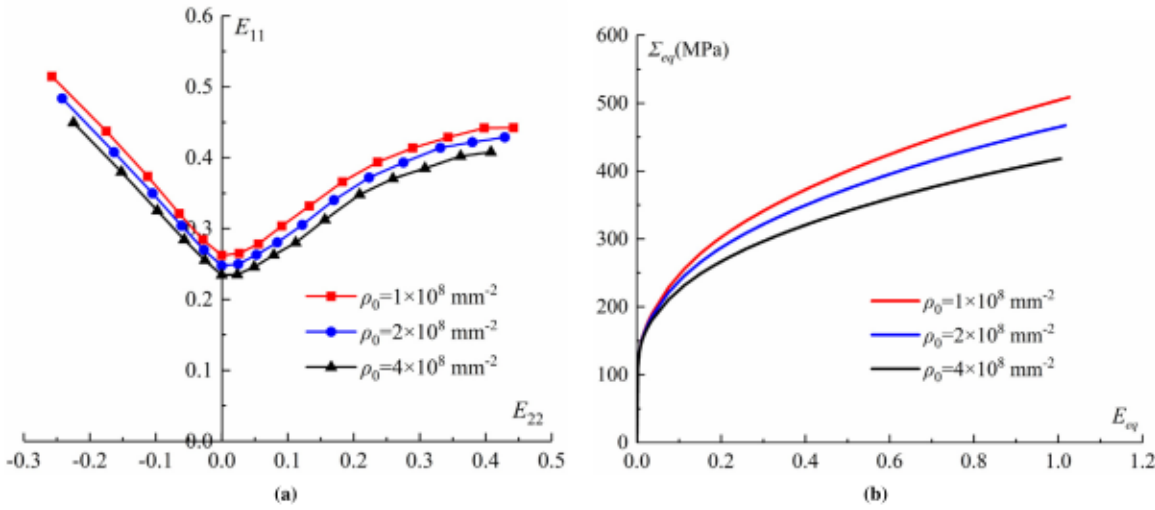

Fig. 11. Effect of the initial dislocation density ρ_0 on: (a) FLD predictions; (b) evolution of the macroscopic equivalent von Mises stress as a function of the macroscopic equivalent strain for strain-path ratio $\rho = -0.5$.

of the Burgers vector, as specified in Table 1). The influence of the critical annihilation distance of dislocations on the ductility limits is evident from Fig. 12(a). One can observe from this figure that the ductility limits significantly decrease as the critical annihilation distance of dislocations increases. Fig. 12(b) provides the evolution of the macroscopic equivalent von Mises stress and the hardening rate defined as $d\Sigma_{eq}/dE_{eq}$ with respect to the macroscopic equivalent strain E_{eq} for the strain-path ratio $\rho = -0.5$. The increase in the critical annihilation distance of dislocations results in a decrease in the hardening rate and the stress level and, subsequently, the ductility limits, as indicated in Fig. 12(b). These findings are consistent with the numerical predictions presented in Franz et al. 2013, where strain localization analysis has been performed using the self-consistent multiscale scheme.

3.2.5. Effect of the dislocation storage parameter K

The impact of the dislocation storage parameter K, related to dislocation generation, on the ductility limits is investigated in this section. The different numerical results are reported in Fig. 13(a). It is clearly highlighted that the predicted ductility limits decrease with the increase in the dislocation storage parameter K for the whole range of strain-path ratios. Furthermore, the evolutions of the macroscopic equivalent von Mises stress and the hardening rate in terms of the macroscopic equivalent strain are plotted in Fig. 13(b). It is shown that the hardening rate and the mechanical strength decrease with an increase in the dislocation storage parameter. Consequently, this leads to lower plastic work-hardening and reduced formability. This observation aligns well with the results reported in Franz et al. (2013).
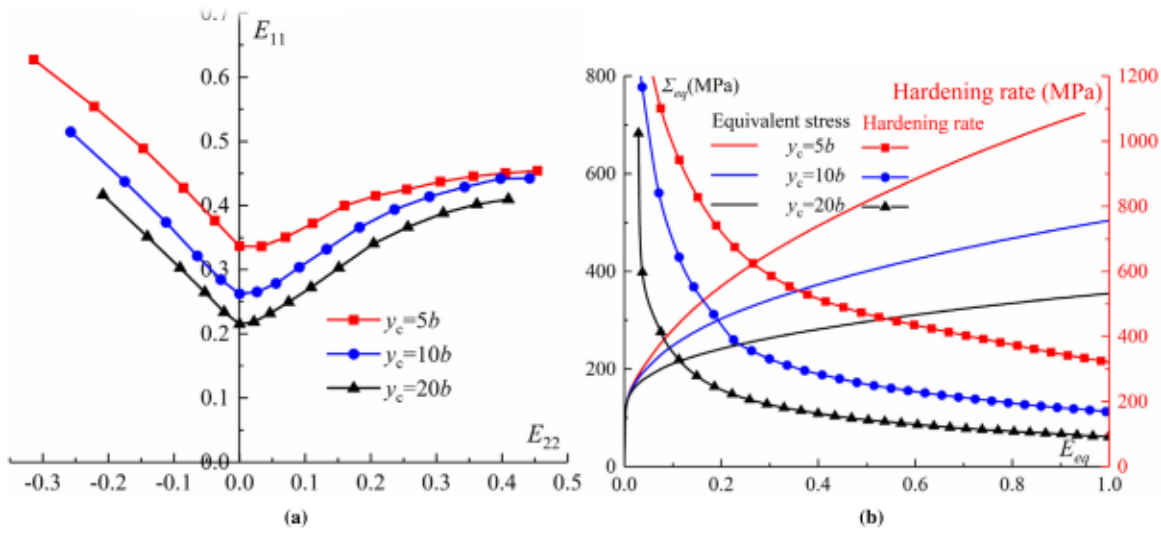
Fig. 12. (a) Effect of the critical annihilation distance of dislocations y_c on the FLD predictions; (b) evolutions of the macroscopic equivalent von Mises stress and the hardening rate as functions of the macroscopic equivalent strain for the strain-path ratio $\rho = -0.5$.
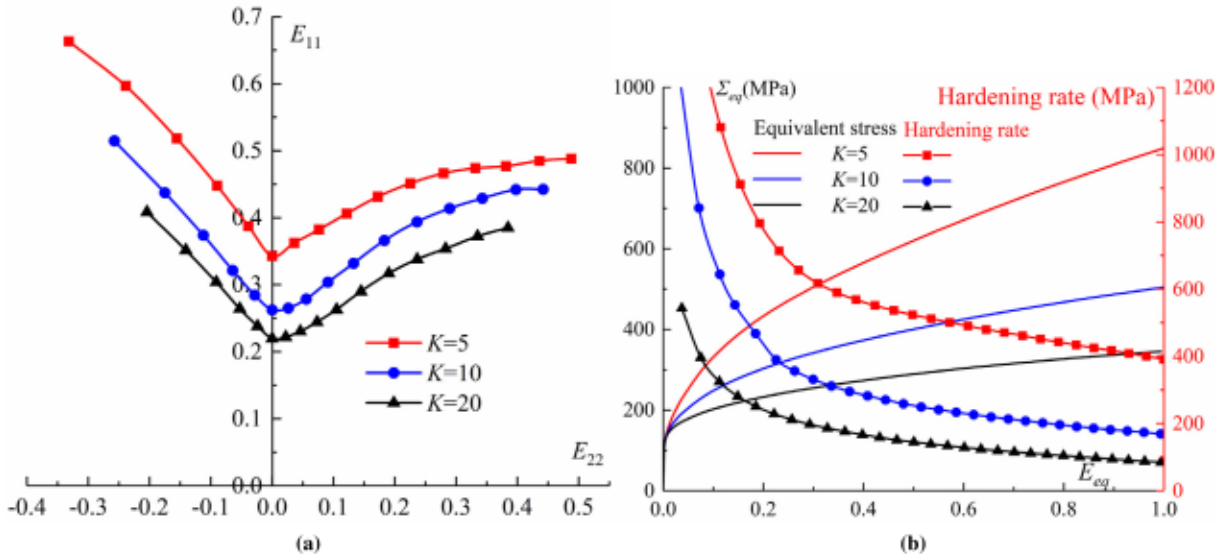

Fig. 13. (a) Effect of the dislocation storage parameter K on the FLD predictions; (b) evolutions of the macroscopic equivalent von Mises stress and the hardening rate as functions of the macroscopic equivalent strain for the strain-path ratio $\rho = -0.5$.

3.2.6. Effect of the kinematic hardening parameter C

The impact of the kinematic hardening parameter C on the shape and level of the FLDs is thoroughly examined in Fig. 14(a)–14(c). In these figures, three different values of C are considered: 100, 200, and 400 MPa, respectively. The numerical results reveal a significant reduction in the predicted ductility limits when kinematic hardening is incorporated in the constitutive modeling, as compared to isotropic hardening, for the whole range of strain-path ratios. Conversely, the disparity between FLD predictions from isotropic and mixed hardening models intensifies as the kinematic hardening parameter C increases for positive strain paths. Brahme et al. (2011) have confirmed that kinematic hardening tends to promote the occurrence of plastic strain localization. For a more comprehensive understanding of the effect of kinematic hardening on the predicted formability, Fig. 14(d) illustrates the relative deviations from the reference ductility limits (obtained from the isotropic hardening model). The calculated relative differences span from 6.2% to 30% for different values of the hardening parameter C. Fig. 14(e) plots the evolution of the macroscopic equivalent von Mises stress with respect to the macroscopic equivalent strain for the strain-path ratio $\rho = -0.5$. It is clearly shown that the mechanical strength increases with the hardening parameter C. Similar conclusions have been reported and discussed in earlier studies by Tvergaard (1978) and Lu and Lee (1987), who predicted the forming limits using both isotropic and kinematic hardening

Table 2
Definition of the different applied pre-strains ρ_1.

Pre-strain path	Pre-strain level	Designation
Uniaxial tension ($\rho_1 = -0.5$)	$E_{11} = 0.05$	UT 0.05
	$E_{11} = 0.10$	UT 0.10
	$E_{11} = 0.15$	UT 0.15
Plane-strain tension ($\rho_1 = 0$)	$E_{11} = 0.05$	PS 0.05
	$E_{11} = 0.10$	PS 0.10
	$E_{11} = 0.15$	PS 0.15
Equibiaxial tension ($\rho_1 = 1$)	$E_{11} = 0.05$	BT 0.05
	$E_{11} = 0.10$	BT 0.10
	$E_{11} = 0.15$	BT 0.15

models (with phenomenological constitutive frameworks). They demonstrated that the consideration of kinematic hardening leads to a reduction in the ductility limits, particularly for positive strain-path ratios ($\rho > 0$). Furthermore, incorporating kinematic hardening into the constitutive modeling allows for better reproduction of the experimental results, as shown in Tvergaard (1978). Additionally, Ben Bettaieb and Abed-Meraim (2017a) have coupled the phenomenological Armstrong–Frederick (A–F) kinematic hardening model with the M–K criterion to predict ductility limit strains for thin substrate-supported metal layers. They have also verified that kinematic hardening clearly decreases the ductility limit strains, particularly in the range of positive strain paths.

3.2.7. Effect of strain path changes

The effect of a pre-strain, which precedes the classical linear strain paths required to determine the FLDs, on the predicted ductility limits is thoroughly analyzed in the present section. To achieve this goal, several pre-strains (denoted as ρ_1), and the subsequent strain paths ρ_2 ranging from -0.5 to 1, with $\Delta\rho = 0.1$, are applied to investigate the effect of the pre-strain path and its level on FLDs. It is worth noting that the transition between the pre-strain ρ_1 and the subsequent strain paths ρ_2 occurs abruptly. The details corresponding to the different applied pre-strains ρ_1 are provided in Table 2.

The unit cell and material parameters used in the FLD predictions under non-linear strain paths (3 pre-strain levels × 3 strain paths) are the same as the ones defined in Section 3.2. The predicted FLDs are plotted in Fig. 15. It is immediately clear that the pre-strain levels significantly affect the predicted limit strains. The numerical simulations suggest that, as the pre-strain levels increase for the uniaxial tension pre-strain path ($\rho_1 = -0.5$), the ductility limits exhibit significant increase for the subsequent strain paths $\rho_2 \geq 0$, as seen in Fig. 15(a). On the other hand, with the increase in the level of the pre-strain path $\rho_1 = 1$, the ductility limits are increased for the subsequent strain paths $\rho_2 \leq 0$ (Fig. 15(c)). As to the case of the pre-strain path $\rho_1 = 0$, increasing its level leads to a slight increase in the predicted subsequent limit strains (Fig. 15(b)). Similar observations have been reported in the literature Yang et al. (2010) and Butuc et al. (2011). Furthermore, it is evident from Fig. 15 that the strain-path transition has a noticeable effect on the predicted ductility limits, particularly when compared to predictions under linear strain paths. These numerical results are in accordance with the previous work of Ma et al. (2018), where the formability of a 5754-O aluminum alloy sheet has been determined using the M–K approach under pre-strain condition.

3.2.8. Effect of the selected multiscale scheme

In this section, the FLDs predicted by the CPFEM are compared to those determined by the well-known full-constraint Taylor model. The latter model assumes a uniform strain distribution across the microstructure, which simplifies the computations, but may overlook local inhomogeneities as the interactions between the different grains are not considered. By contrast, the periodic homogenization scheme accounts for the spatial (periodic) variation of strain field within the microstructure by applying periodic boundary conditions (PBCs) on the nodes of two opposite surfaces of the RVE (see Sections 2.3 and 3.2.1). The application of such boundary conditions leads to potentially more accurate predictions of the macroscopic plastic behavior and, consequently, of the onset of localized necking. The differences in boundary conditions between the two multiscale schemes result in different expressions of the macroscopic tangent modulus $\mathbf{C}$, which is required to predict strain localization by the bifurcation theory. Specifically, when the periodic homogenization scheme is used, the macroscopic tangent modulus $\mathbf{C}$ is computed by Eq. (45). However, when the Taylor model is adopted, the macroscopic tangent modulus $\mathbf{C}$ is obtained by the following expression:

$$\mathbf{C} = \frac{1}{|V_0|}\mathbb{Q} \cdot \mathbf{K} \cdot \mathbb{Q}^T. \tag{53}$$

The impact of the selected multiscale scheme on the predicted FLDs is evident, as illustrated in Fig. 16. Our findings reveal that the limit strains predicted by both multiscale schemes exhibit nearly identical shapes and levels in the range of negative strain paths ($\rho \leq 0$). However, for positive strain paths, the limit strains predicted by the Taylor model are significantly lower than those predicted by the CPFEM. Similar conclusions have been drawn by Nagra et al. (2018), emphasizing that the Taylor model tends to underestimate the limit strains of AA3003-O sheets for the whole range of strain paths, as compared to the predictions of the FFT model (similar to the CPFEM approach used in the present study). Nagra et al. (2018) also found that the limit strains of AA5754-O sheets predicted by the Taylor model are much lower than those obtained by the FFT model for $\rho > 0$, while almost identical forming limits are predicted by both models for $\rho \leq 0$. Additionally, the authors show that the limit strains predicted by the FFT model closely align with experimental data. Furthermore, Signorelli et al. (2009) have investigated the effect of the multiscale scheme strategy
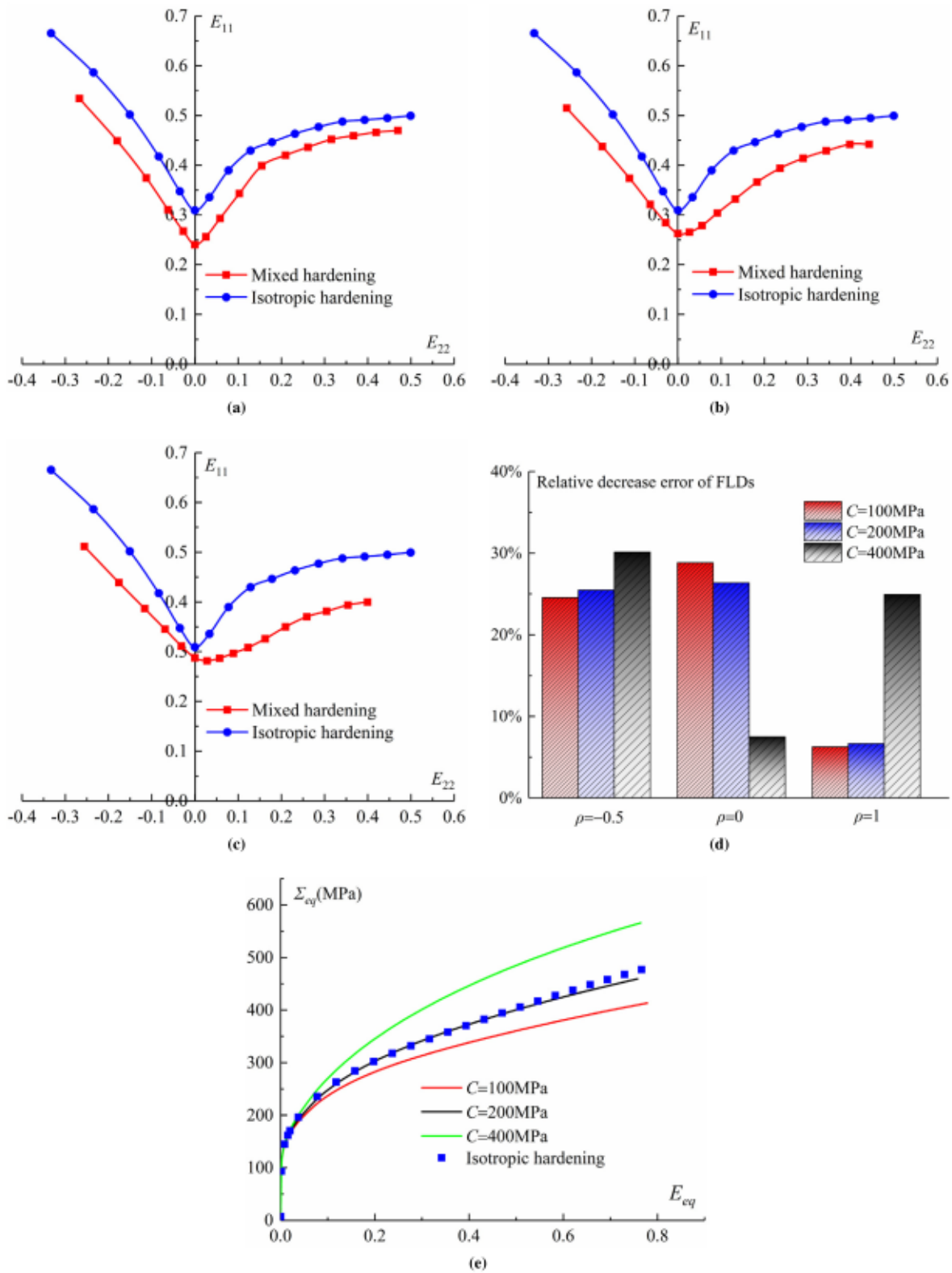
Fig. 14. Effect of the kinematic hardening parameter C on the FLD predictions: (a) $C = 100$ MPa; (b) $C = 200$ MPa; (c) $C = 400$ MPa; (d) relative decrease error of FLDs for strain-path ratios $\rho = -0.5$, $\rho = 0$ and $\rho = 1$; (e) evolution of the macroscopic equivalent von Mises stress as a function of the macroscopic equivalent strain for the strain-path ratio $\rho = -0.5$ with different hardening models and parameters.
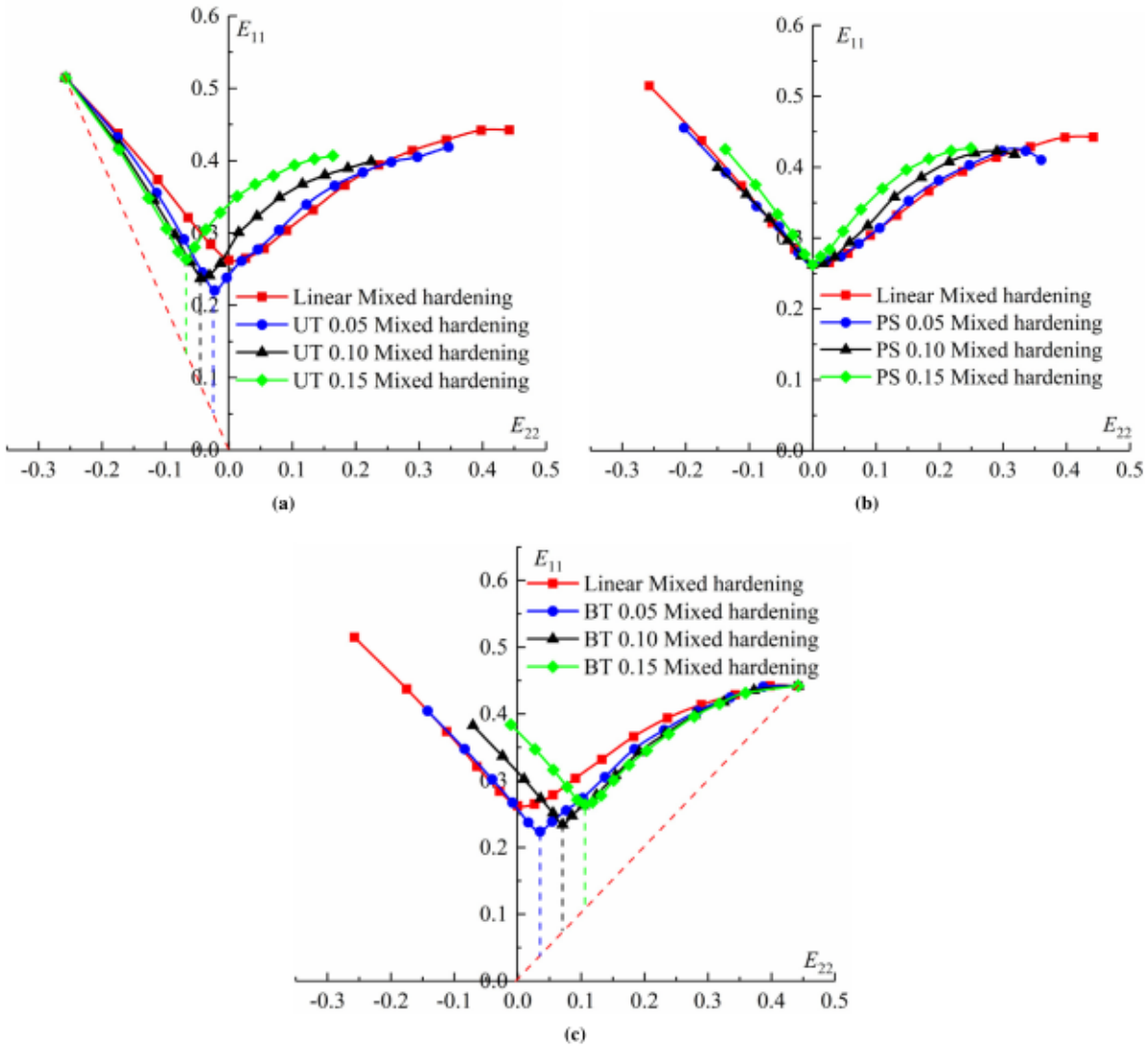
Fig. 15. Effect of pre-strain loading path on the predicted FLDs using the mixed hardening model for: (a) uniaxial tension pre-strain (UT); (b) plane-strain pre-strain (PS); (c) equibiaxial tension pre-strain (BT).

on the predicted FLDs. Their simulation results show that the full-constraint Taylor model predicts lower limit strains than those obtained by the viscoplastic self-consistent (VPSC) model for the whole range of strain-paths. More recently, Serenelli et al. (2011) have also demonstrated that the full-constraint Taylor model provides significantly lower forming limits on the right-hand side of the FLD ($\rho > 0$) for a typical FCC material, as compared to experimental data. It should be noted that the forming limits in these contributions (Signorelli et al., 2009; Serenelli et al., 2011; Nagra et al., 2018) have been determined by the M–K approach.

3.2.9. Comparison with experimental data of Nicoletti et al. (2023)

To emphasize the predictive capability of the proposed computational strategy, the numerical results are compared to the experimental data provided in Nicoletti et al. (2023). For this purpose, the material parameters, used as inputs for the numerical predictions, are identified on the basis of the experimental uniaxial tension response corresponding to the AA6061-T4 aluminum alloy sheet presented in Nicoletti et al. (2023). Fig. 17(a) highlights the accuracy of the identification procedure. The identified material parameters are listed in Table 3, and the other parameters are kept the same as those provided in Table 1. The FLD predicted by the proposed computational strategy is depicted in Fig. 17(b) along with the experimental data published in Nicoletti et al. (2023). As clearly shown in this figure, the predicted limit strains are slightly higher than their experimental counterparts. This outcome is expected, as it is well known that the FLDs predicted by the Rice bifurcation theory represent an upper bound to the experimentally measured necking strains. This result reaffirms a similar conclusion reported in the literature (Chalal and Abed-Meraim, 2017, among others). It is important to note that the experimental data is determined using the Marciniak test based
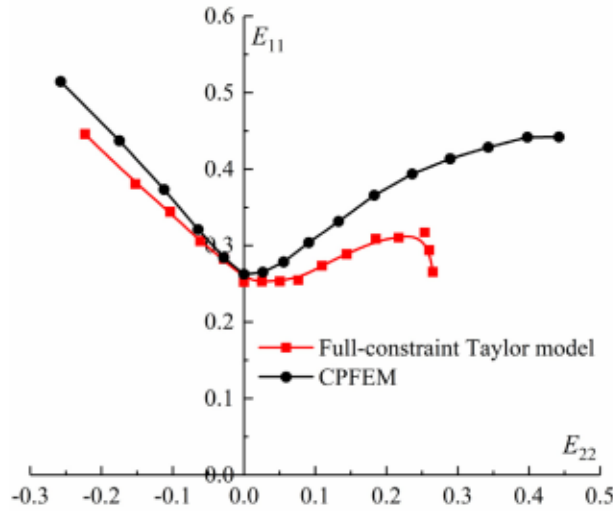
Fig. 16. Effect of the selected multiscale scheme on the predicted FLDs.

Table 3
The identified material parameters used for the numerical simulations.

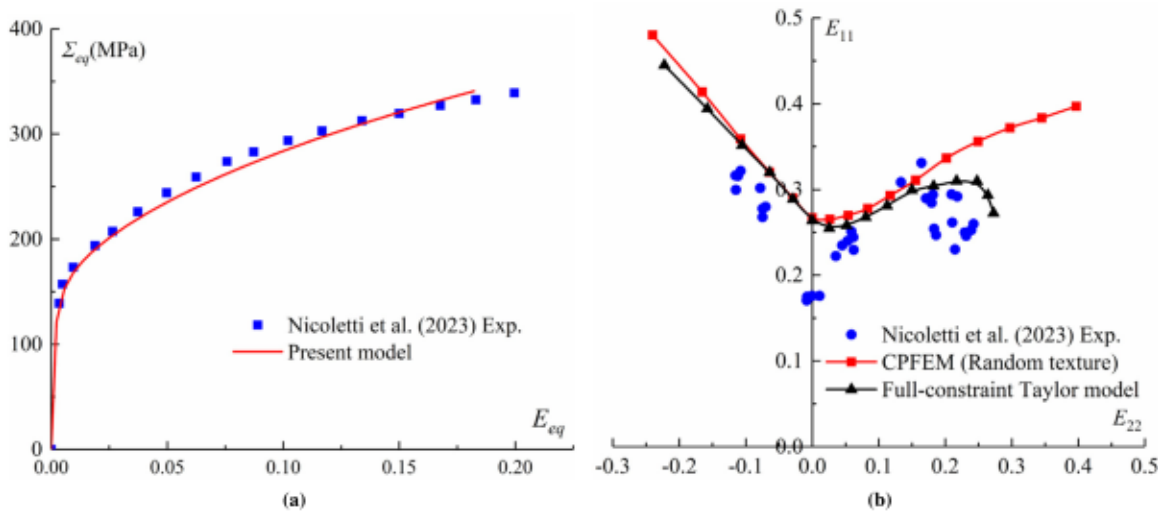| E (GPa)	μ (GPa)	τ_0 (MPa)	b (mm)	y_c	C (MPa)
70	26.923	58	3.26×10^{-7}	$12b$	400

Fig. 17. Comparison of the numerical predictions with the experimental data provided in Nicoletti et al. (2023): (a) experimental and fitted macroscopic equivalent von Mises stress–strain responses under uniaxial tension loading; (b) experimental and predicted ductility limit strains.

on the ISO 12004-2:2008 norm, and these experimental points correspond to 'safe limit strains' as explained in Nicoletti et al. (2023). Also, the FLD predicted by the full-constraint Taylor model is included to Fig. 17(b). Although the limit strains predicted by the Taylor model align more closely with the experimental data in the range of biaxial strain paths, some important factors (such as the grain boundary effect, the initial geometric imperfections unavoidably present in real sheets, or the specific sheet forming experimental conditions) cannot be accounted for in the current predictions. In view of the discussions above, it comes that overall, our numerical prediction strategy does not significantly overestimate the forming limit strains.

3.2.10. Effect of the initial crystallographic texture

To investigate the effect of the initial crystallographic texture on the predicted ductility limits, we have selected an actual material texture corresponding to the AA6061-T4 aluminum alloy sheet, as detailed in Nicoletti et al. (2023). This actual texture comprises 3000 crystallographic orientations. From this set of 3000 orientations, we have carefully selected the 200 most representative
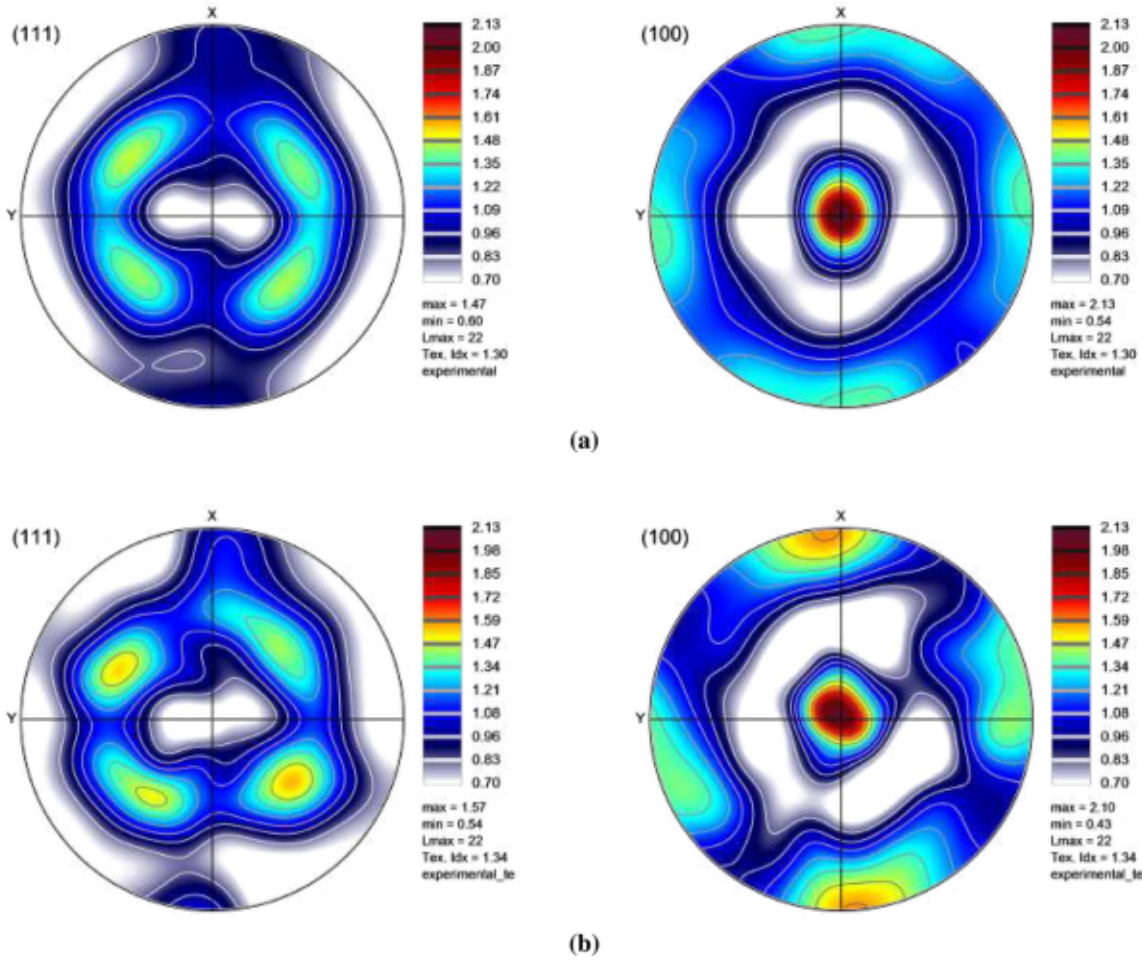
Fig. 18. (111) and (100) pole figures of the initial crystallographic textures: (a) 3000 experimental crystallographic orientations provided by Nicoletti et al. (2023); (b) 200 discrete orientations used as input of the numerical predictions.

orientations. This selection ensures that the two crystallographic textures, the one with 3000 experimental orientations and the other with 200 orientations, exhibit very similar (111) and (100) pole figures. Fig. 18 visually demonstrates the close similarity between the (111) and (100) pole figures corresponding to the 3000 orientations discretized from the experimental data of Nicoletti et al. (2023) and to the 200 discrete orientations, which will be used as input for our numerical predictions.

Fig. 19 compares the limit strains predicted using the random texture presented in Fig. 3(c) with those obtained using the actual texture defined by the 200 discrete orientations as depicted in Fig. 18(b). As expected, the initial crystallographic texture has an appreciable effect on the predicted forming limits. It is clear from Fig. 19 that the forming limit strains predicted by the actual texture are slightly higher than those obtained using the random texture for $\rho \leq 0$. On the other hand, the difference between the limit strains predicted by the actual texture and those given by the random texture is more significant for $\rho > 0$. This discrepancy can be attributed to the inclusion of 7% cube and 4.7% rotated cube textures in the actual texture. Indeed, several studies (Yoshida et al., 2007; Zhu et al., 2023b, among others) have demonstrated that cube texture yields forming limits that are much higher than those obtained by random textures in the biaxial stretching range ($\rho > 0$). Consequently, our predictions are not overly conservative in the biaxial tension range, when compared to those obtained using the actual texture.

4. Summary and concluding remarks

In this work, we have incorporated a physically-based isotropic-kinematic hardening model into a finite strain crystal plasticity framework with the aim of predicting the ductility limits of thin metal sheets. To achieve this goal, we have used unit cells representing the studied thin metal sheets and applied the periodic homogenization scheme to derive the unit cell mechanical behavior from that of the constituent single crystals. The mechanical behavior of each single crystal is assumed to be elastoplastic with physically-based isotropic-kinematic hardening, and with a plastic flow rule modeled by the classical Schmid law. The dislocation density evolution law, initially formulated by Kocks (Kocks, 1976), is introduced to describe isotropic hardening, whereas
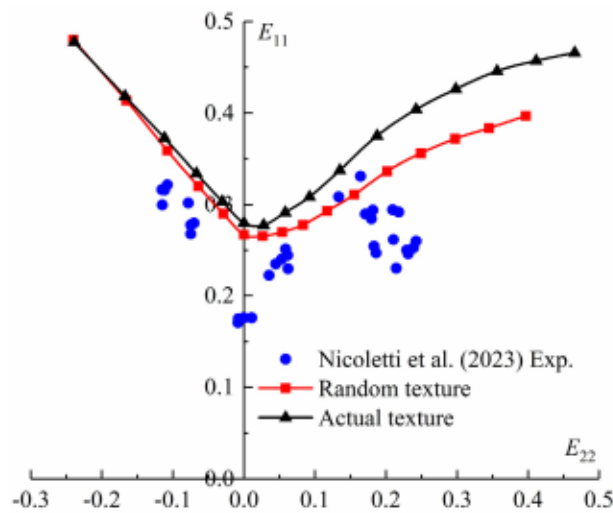
Fig. 19. Effect of the initial crystallographic texture on the predicted FLDs.

kinematic hardening is modeled using the typical nonlinear Armstrong–Frederick (A–F) law. The constitutive equations at the single crystal scale are implemented within the ABAQUS/Standard finite element code using a User-defined MATerial subroutine (UMAT). The Rice bifurcation criterion is adopted to detect the initiation of localized necking. Several simulations have been carried out to evaluate the reliability of the selected hardening models. The major findings and conclusions drawn from this work are summarized as follows:

- Based on several sensitivity studies, we have demonstrated that the initial dislocation density, the critical annihilation distance of dislocations, and the dislocation storage parameter have remarkable impacts on the predicted forming limit diagrams (FLDs) (Figs. 11–13). The outcomes of these sensitivity analyses suggest that controlling these physical factors at lower levels through microstructural adjustments may enhance ductility.
- The introduction of kinematic hardening into the single crystal constitutive modeling leads to a notable reduction in the predicted ductility limits compared to isotropic hardening, as depicted in Fig. 14. Furthermore, the comparison of the forming limits predicted by the present model with experimental data shows that the consideration of kinematic hardening allows more accurate predictions of the ductility limits.
- The ductility limits obtained under non-linear strain paths are deeply investigated, where the non-linear strain paths are composed of two sequential linear strain paths, and the first linear loading stage is either the uniaxial tensile state (UT), plane-strain tensile state (PS), or equibiaxial tensile state (BT). Our findings show that the predicted limit strains are significantly influenced by the strain-path changes, as illustrated in Fig. 15. Furthermore, our predictions are found to be similar to the experimental and numerical results obtained by the classical phenomenological constitutive model and reported in Ma et al. (2018).
- The application of the full-constraint Taylor model to predict material ductility yields forming limit strains that are much lower than those obtained by the present CPFEM-based multiscale scheme, especially in the range of positive strain-path ratios (Fig. 16).
- The comparative analyses of forming limit predictions based on actual textures and those obtained with random textures reveal the important role played by the initial crystallographic texture in the prediction of ductility limits (Fig. 19).

CRediT authorship contribution statement

S. Zhou: Writing – original draft, Validation, Software, Methodology, Investigation, Data curation. **M. Ben Bettaieb:** Writing – review & editing, Supervision, Software, Methodology, Investigation. **F. Abed-Meraim:** Writing – review & editing, Supervision, Software, Methodology.

Declaration of competing interest

The authors declare that they have no known competing financial interests or personal relationships that could have appeared to influence the work reported in this paper.

Data availability

No data was used for the research described in the article.

Table A.1
Crystallographic slip system numbering for FCC single crystals.

α	1	2	3	4	5	6	7	8	9	10	11	12
$\sqrt{3}\,\vec{n}_0^{\alpha}$	$\left\{\begin{matrix}1\\1\\1\end{matrix}\right\}$	$\left\{\begin{matrix}1\\1\\1\end{matrix}\right\}$	$\left\{\begin{matrix}1\\1\\1\end{matrix}\right\}$	$\left\{\begin{matrix}-1\\1\\1\end{matrix}\right\}$	$\left\{\begin{matrix}-1\\1\\1\end{matrix}\right\}$	$\left\{\begin{matrix}-1\\1\\1\end{matrix}\right\}$	$\left\{\begin{matrix}1\\-1\\1\end{matrix}\right\}$	$\left\{\begin{matrix}1\\-1\\1\end{matrix}\right\}$	$\left\{\begin{matrix}1\\-1\\1\end{matrix}\right\}$	$\left\{\begin{matrix}1\\1\\-1\end{matrix}\right\}$	$\left\{\begin{matrix}1\\1\\-1\end{matrix}\right\}$	$\left\{\begin{matrix}1\\1\\-1\end{matrix}\right\}$
$\sqrt{2}\,\vec{m}_0^{\alpha}$	$\left\{\begin{matrix}1\\-1\\0\end{matrix}\right\}$	$\left\{\begin{matrix}1\\0\\-1\end{matrix}\right\}$	$\left\{\begin{matrix}0\\1\\-1\end{matrix}\right\}$	$\left\{\begin{matrix}1\\1\\0\end{matrix}\right\}$	$\left\{\begin{matrix}1\\0\\1\end{matrix}\right\}$	$\left\{\begin{matrix}0\\1\\1\end{matrix}\right\}$	$\left\{\begin{matrix}1\\1\\0\end{matrix}\right\}$	$\left\{\begin{matrix}1\\0\\1\end{matrix}\right\}$	$\left\{\begin{matrix}0\\1\\-1\end{matrix}\right\}$	$\left\{\begin{matrix}1\\-1\\0\end{matrix}\right\}$	$\left\{\begin{matrix}1\\0\\1\end{matrix}\right\}$	$\left\{\begin{matrix}0\\1\\1\end{matrix}\right\}$

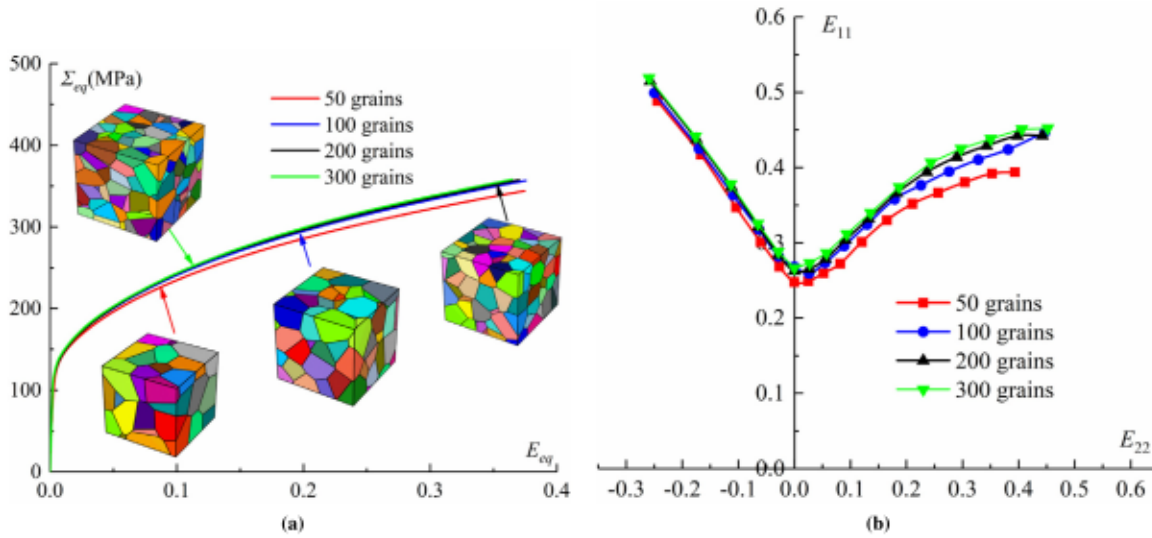**Fig. B.1.** Effect of the grain number on: (a) the macroscopic equivalent von Mises stress–strain response; (b) FLD predictions.

Appendix A. Crystallographic slip systems for FCC single crystals

The 12 slip systems of FCC single crystals are provided in Table A.1. Each slip system is described by orthonormal vectors $\left(\vec{m}_0^{\alpha}, \vec{n}_0^{\alpha}\right)$ and both vectors are measured in the intermediate configuration.

Appendix B. Grain number sensitivity study

A sensitivity study on grain number has been conducted to determine an adequate number of grains for statistically representing the studied materials. Fig. B.1(a) depicts the macroscopic equivalent von Mises stress–strain response, under uniaxial tension test, for unit cells containing 50, 100, 200 and 300 grains. The predicted FLDs corresponding to different grain numbers are provided in Fig. B.1(b). The results from this study indicate that the tensile responses for unit cells containing 100, 200, and 300 grains are almost indistinguishable, and the difference between the FLDs predicted by unit cells containing 200 and 300 grains is very small. Therefore, we can consider that unit cells comprising at least 200 grains may be sufficient to adequately represent the polycrystalline materials in the current study. It is also well acknowledged that the determination of a sufficient number of grains is intricately linked to factors, such as the adopted hardening model, homogenization method, among others.

References

Agaram, S., Kanjarla, A.K., Bhuvaraghan, B., Srinivasan, S.M., 2021. Dislocation density based crystal plasticity model incorporating the effect of precipitates in IN718 under monotonic and cyclic deformation. Int. J. Plast. 141, 102990. http://dx.doi.org/10.1016/j.ijplas.2021.102990.

Akpama, H.K., Ben Bettaieb, M., Abed-Meraim, F., 2016. Numerical integration of rate-independent BCC single crystal plasticity models: comparative study of two classes of numerical algorithms. Internat. J. Numer. Methods Engrg. 108 (5), 363–422. http://dx.doi.org/10.1002/nme.5215.

Akpama, H.K., Ben Bettaieb, M., Abed-Meraim, F., 2017. Localized necking predictions based on rate-independent self-consistent polycrystal plasticity: Bifurcation analysis versus imperfection approach. Int. J. Plast. 91, 205–237. http://dx.doi.org/10.1016/j.ijplas.2017.02.001.

Armstrong, P.J., Frederick, C., 1966. A mathematical representation of the multiaxial Bauschinger effect, vol. 731, Central Electricity Generating Board, Report RD/B/N731, 1, Berkely Nuclear Laboratories, Berkely, UK..

Banerjee, B., Bhawalkar, A.S., 2008. An extended mechanical threshold stress plasticity model: Modeling 6061-T9 aluminum alloy. J. Mech. Mater. Struct. 3 (3), 391–424. http://dx.doi.org/10.2140/jomms.2008.3.391.

Beausir, B., Fundenberger, J.-J., 2017. Analysis tools for electron and X-ray diffraction, ATEX - software, www.atex-software.eu. Univ. Lorraine - Metz.

Ben Bettaieb, M., Abed-Meraim, F., 2015. Investigation of localized necking in substrate-supported metal layers: Comparison of bifurcation and imperfection analyses. Int. J. Plast. 65, 168–190. http://dx.doi.org/10.1016/j.ijplas.2014.09.003.

Ben Bettaieb, M., Abed-Meraim, F., 2017a. Effect of kinematic hardening on localized necking in substrate-supported metal layers. Int. J. Mech. Sci. 123, 177–197. http://dx.doi.org/10.1016/j.ijmecsci.2016.12.002.

Ben Bettaieb, M., Abed-Meraim, F., 2017b. Localized necking in elastomer-supported metal layers: impact of kinematic hardening. J. Manuf. Sci. Eng. Trans. ASME 139 (6), http://dx.doi.org/10.1115/1.4035183.

Ben Bettaieb, M., Débordes, O., Dogui, A., Duchêne, L., Keller, C., 2012. On the numerical integration of rate independent single crystal behavior at large strain. Int. J. Plast. 32–33, 184–217. http://dx.doi.org/10.1016/j.ijplas.2011.10.010.

Bonatti, C., Mohr, D., 2021. Neural network model predicting forming limits for bi-linear strain paths. Int. J. Plast. 137, 102886. http://dx.doi.org/10.1016/j.ijplas.2020.102886.

Bong, H.J., Lee, J., 2021. Crystal plasticity finite element-Marciniak-Kuczynski approach with surface roughening effect in predicting formability of ultra-thin ferritic stainless steel sheets. Int. J. Mech. Sci. 191, 106066. http://dx.doi.org/10.1016/j.ijmecsci.2020.106066.

Bong, H.J., Lee, J., Hu, X., Sun, X., Lee, M.G., 2020. Predicting forming limit diagrams for magnesium alloys using crystal plasticity finite elements. Int. J. Plast. 126, 102630. http://dx.doi.org/10.1016/j.ijplas.2019.11.009.

Brahme, A.P., Inal, K., Mishra, R.K., Saimoto, S., 2011. The backstress effect of evolving deformation boundaries in fcc polycrystals. Int. J. Plast. 27 (8), 1252–1266. http://dx.doi.org/10.1016/j.ijplas.2011.02.006.

Bratov, V., Borodin, E.N., 2015. Comparison of dislocation density based approaches for prediction of defect structure evolution in aluminium and copper processed by ECAP. Mater. Sci. Eng. A 631, 10–17. http://dx.doi.org/10.1016/j.msea.2015.02.019.

Butuc, M.C., Teodosiu, C., Barlat, F., Gracio, J.J., 2011. Analysis of sheet metal formability through isotropic and kinematic hardening models. Eur. J. Mech. A Solids 30 (4), 532–546. http://dx.doi.org/10.1016/j.euromechsol.2011.03.005.

Chalal, H., Abed-Meraim, F., 2017. Determination of forming limit diagrams based on ductile damage models and necking criteria. Lat. Am. J. Solids Struct. 14 (10), 1872–1892. http://dx.doi.org/10.1590/1679-78253481.

Dong, Y., He, X., Zhang, Z., 2020. A new crystal plasticity modeling of uniaxial ratcheting behavior for face-centered cubic 6061 aluminum alloy. Mater. Res. Express 7 (10), http://dx.doi.org/10.1088/2053-1591/abbdee.

Dong, Y., Kang, G., Yu, C., 2014. A dislocation-based cyclic polycrystalline visco-plastic constitutive model for ratchetting of metals with face-centered cubic crystal structure. Comput. Mater. Sci. 91, 75–82. http://dx.doi.org/10.1016/j.commatsci.2014.04.030.

Farooq, H., Cailletaud, G., Forest, S., Ryckelynck, D., 2020. Crystal plasticity modeling of the cyclic behavior of polycrystalline aggregates under non-symmetric uniaxial loading: Global and local analyses. Int. J. Plast. 126, 102619. http://dx.doi.org/10.1016/j.ijplas.2019.10.007.

Franz, G., Abed-Meraim, F., Berveiller, M., 2013. Strain localization analysis for single crystals and polycrystals: Towards microstructure-ductility linkage. Int. J. Plast. 48, 1–33. http://dx.doi.org/10.1016/j.ijplas.2013.02.001.

Geuzaine, C., Remacle, J.-F., 2009. Gmsh: A 3-D finite element mesh generator with built-in pre- and post-processing facilities. Internat. J. Numer. Methods Engrg. 79 (11), 1309–1331. http://dx.doi.org/10.1002/nme.2579.

Goodwin, G., 1968. Application of strain analysis to sheet metal forming problems in the press shop. SAE Pap. 77, 380–387. http://dx.doi.org/10.4271/680093.

Gupta, A., Ben Bettaieb, M., Abed-Meraim, F., Kalidindi, S.R., 2018. Computationally efficient predictions of crystal plasticity based forming limit diagrams using a spectral database. Int. J. Plast. 103, 168–187. http://dx.doi.org/10.1016/j.ijplas.2018.01.007.

Haddag, B., Abed-Meraim, F., Balan, T., 2009. Strain localization analysis using a large deformation anisotropic elastic-plastic model coupled with damage. Int. J. Plast. 25 (10), 1970–1996. http://dx.doi.org/10.1016/j.ijplas.2008.12.013.

Han, F., Roters, F., Raabe, D., 2020. Microstructure-based multiscale modeling of large strain plastic deformation by coupling a full-field crystal plasticity-spectral solver with an implicit finite element solver. Int. J. Plast. 125, 97–117. http://dx.doi.org/10.1016/j.ijplas.2019.09.004.

Haouala, S., Segurado, J., LLorca, J., 2018. An analysis of the influence of grain size on the strength of fcc polycrystals by means of computational homogenization. Acta Mater. 148, 72–85. http://dx.doi.org/10.1016/j.actamat.2018.01.024, arXiv:1801.05155.

Harder, J., 1999. Crystallographic model for the study of local deformation processes in polycrystals. Int. J. Plast. 15 (6), 605–624. http://dx.doi.org/10.1016/S0749-6419(99)00002-9.

Hennessey, C., Castelluccio, G.M., McDowell, D.L., 2017. Sensitivity of polycrystal plasticity to slip system kinematic hardening laws for Al 7075-T6. Mater. Sci. Eng. A 687, 241–248. http://dx.doi.org/10.1016/j.msea.2017.01.070.

Hou, Y., Lee, M.G., Lin, J., Min, J., 2022. Experimental characterization and modeling of complex anisotropic hardening in quenching and partitioning (Q&P) steel subject to biaxial non-proportional loadings. Int. J. Plast. 156, 103347. http://dx.doi.org/10.1016/j.ijplas.2022.103347.

Hutchinson, J.W., Neale, K.W., 1978. Sheet necking-II. Time-independent behavior. In: Mechanics of Sheet Metal Forming. pp. 127–153. http://dx.doi.org/10.1007/978-1-4613-2880-3_6.

Keeler, S.P., Backhofen, W.A., 1963. Plastic instability and fracture in sheets stretched over rigid punches. ASM Trans. Q. 56, 25–48.

Kim, J.H., Lee, M.G., Kang, J.H., Oh, C.S., Barlat, F., 2017. Crystal plasticity finite element analysis of ferritic stainless steel for sheet formability prediction. Int. J. Plast. 93, 26–45. http://dx.doi.org/10.1016/j.ijplas.2017.04.007.

Kocks, U., 1976. Laws for work-hardening and low-temperature creep. J. Eng. Mater. Technol. 98 (1), 76–85. http://dx.doi.org/10.1115/1.3443340.

Le Pécheur, A., Curtit, F., Clavel, M., Stephan, J.M., Rey, C., Bompard, P., 2012. Polycrystal modelling of fatigue: Pre-hardening and surface roughness effects on damage initiation for 304L stainless steel. Int. J. Fatigue 45, 48–60. http://dx.doi.org/10.1016/j.ijfatigue.2012.06.014.

Lejeunes, S., Bourgeois, S., 2011. Une toolbox abaqus pour le calcul de propriétés effectives de milieux hétérogènes. In: 10e Colloq. Natl. en Calc. des Struct.. Giens, France, pp. 1–9.

Lin, J., Hou, Y., Min, J., Tang, H., Carsley, J.E., Stoughton, T.B., 2020. Effect of constitutive model on springback prediction of MP980 and AA6022-T4. Int. J. Mater. Form. 13 (1), http://dx.doi.org/10.1007/s12289-018-01468-x.

Lu, P., Ge, Y., Jin, X., Li, P., Ji, X., Zhao, D., Wang, Z., Fan, X., 2022. A dislocation density-based model for the temperature dependent anomalous behaviors of nickel-based single-crystal superalloy. Mech. Mater. 170, 104326. http://dx.doi.org/10.1016/j.mechmat.2022.104326.

Lu, Z.H., Lee, D., 1987. Prediction of history-dependent forming limits by applying different hardening models. Int. J. Mech. Sci. 29 (2), 123–137. http://dx.doi.org/10.1016/0020-7403(87)90047-6.

Lu, J., Sun, W., Becker, A., 2016. Material characterisation and finite element modelling of cyclic plasticity behaviour for 304 stainless steel using a crystal plasticity model. Int. J. Mech. Sci. 105, 315–329. http://dx.doi.org/10.1016/j.ijmecsci.2015.11.024.

Luo, J., Kang, G., Shi, M., 2013. Simulation to the cyclic deformation of polycrystalline aluminum alloy using crystal plasticity finite element method. Int. J. Comput. Mater. Sci. Eng. 2 (3–4), 1–10. http://dx.doi.org/10.1142/S204768411350019X.

Ma, B.L., Wan, M., Cai, Z.Y., Yuan, W.N., Li, C., Wu, X.D., Liu, W., 2018. Investigation on the forming limits of 5754-O aluminum alloy sheet with the numerical Marciniak-Kuczynski approach. Int. J. Mech. Sci. 142–143, 420–431. http://dx.doi.org/10.1016/j.ijmecsci.2018.05.013.

Marciniak, Z., Kuczyński, K., 1967. Limit strains in the processes of stretch-forming sheet metal. Int. J. Mech. Sci. 9 (9), 609–620. http://dx.doi.org/10.1016/0020-7403(67)90066-5.

Meng, F., 2020. Simulations à l'échelle mesoscopic du comportement en fatigue de métaux CFC (Ph.D. thesis). Université Grenoble Alpes, URL https://tel.archives-ouvertes.fr/tel-03116144.

Miehe, C., 2003. Computational micro-to-macro transitions for discretized micro-structures of heterogeneous materials at finite strains based on the minimization of averaged incremental energy. Comput. Methods Appl. Mech. Engrg. 192 (5), 559–591. http://dx.doi.org/10.1016/S0045-7825(02)00564-9.

Mohammadnejad, S., Basti, A., Ansari, R., 2021. The effect of dislocation density on forming limit curve. Amirkabir J. Mech. Eng. 52 (10), 673–676. http://dx.doi.org/10.22060/mej.2019.15728.6189.

Nagra, J.S., Brahme, A., Mishra, R., Lebensohn, R.A., Inal, K., 2018. An efficient full-field crystal plasticity-based M–K framework to study the effect of 3D microstructural features on the formability of polycrystalline materials. Modelling Simul. Mater. Sci. Eng. 26 (7), 75002. http://dx.doi.org/10.1088/1361-651x/aadc20.

Nicoletti, E.A., Stout, M.G., Bertinetti, M.A., Signorelli, J.W., 2023. A theoretical and experimental study of predicting forming-limit diagrams for face-centered cubic, body-centered cubic and hexagonal close-packed metals using the Marciniak-Kuczynski visco-plastic self-consistent model. J. Mater. Eng. Perform. http://dx.doi.org/10.1007/s11665-023-08905-2.

Qin, J., Holmedal, B., Hopperstad, O.S., 2018. A combined isotropic, kinematic and distortional hardening model for aluminum and steels under complex strain-path changes. Int. J. Plast. 101, 156–169. http://dx.doi.org/10.1016/j.ijplas.2017.10.013.

Quey, R., Dawson, P.R., Barbe, F., 2011. Large-scale 3D random polycrystals for the finite element method: Generation, meshing and remeshing. Comput. Methods Appl. Mech. Engrg. 200 (17), 1729–1745. http://dx.doi.org/10.1016/j.cma.2011.01.002.

Rice, J., 1976. The localization of plastic deformation. In: 14th International Congress of Theoretical and Applied Mechanics. pp. 207–220.

Serenelli, M.J., Bertinetti, M.A., Signorelli, J.W., 2011. Study of limit strains for FCC and BCC sheet metal using polycrystal plasticity. Int. J. Solids Struct. 48 (7–8), 1109–1119. http://dx.doi.org/10.1016/j.ijsolstr.2010.12.013.

Signorelli, J.W., Bertinetti, M.A., Turner, P.A., 2009. Predictions of forming limit diagrams using a rate-dependent polycrystal self-consistent plasticity model. Int. J. Plast. 25 (1), 1–25. http://dx.doi.org/10.1016/j.ijplas.2008.01.005.

Teodosiu, C., Hu, Z., 1995. Evolution of the intragranular microstructure at moderate and large strains: modelling and computational significance. In: Proceedings of the NUMIFORM' 95. pp. 173–182.

Teodosiu, C., Hu, Z., 1998. Microstructure in the continuum modeling of plastic anisotropy. pp. 285–290.

Tvergaard, V., 1978. Effect of kinematic hardening on localized necking in biaxially stretched sheets. Int. J. Mech. Sci. 20 (9), 651–658. http://dx.doi.org/10.1016/0020-7403(78)90023-1.

Yang, M., Dong, X., Zhou, R., Cao, J., 2010. Crystal plasticity-based forming limit prediction for FCC materials under non-proportional strain-path. Mater. Sci. Eng. A 527 (24–25), 6607–6613. http://dx.doi.org/10.1016/j.msea.2010.06.063.

Yoshida, K., 2022. An alternative formulation of two-grain cluster model for homogenization of elastoviscoplastic behavior of polycrystal. Int. J. Plast. 156, 103368. http://dx.doi.org/10.1016/j.ijplas.2022.103368.

Yoshida, K., Brenner, R., Bacroix, B., Bouvier, S., 2009. Effect of regularization of schmid law on self-consistent estimates for rate-independent plasticity of polycrystals. Eur. J. Mech. A Solids 28 (5), 905–915. http://dx.doi.org/10.1016/j.euromechsol.2009.05.001.

Yoshida, K., Ishizaka, T., Kuroda, M., Ikawa, S., 2007. The effects of texture on formability of aluminum alloy sheets. Acta Mater. 55 (13), 4499–4506. http://dx.doi.org/10.1016/j.actamat.2007.04.014.

Yoshida, K., Kuroda, M., 2012. Comparison of bifurcation and imperfection analyses of localized necking in rate-independent polycrystalline sheets. Int. J. Solids Struct. 49 (15–16), 2073–2084. http://dx.doi.org/10.1016/j.ijsolstr.2012.04.010.

Zhou, D., Wang, X., Wang, R., Zhang, T., Yang, X., Jiang, Y., Zhang, X., Gong, J., Tu, S., 2022. An extended crystal plasticity model to simulate the deformation behaviors of hybrid stress-strain controlled creep-fatigue interaction loading. Int. J. Fatigue 156, 106680. http://dx.doi.org/10.1016/j.ijfatigue.2021.106680.

Zhu, J.C., Ben Bettaieb, M., Abed-Meraim, F., 2020a. Investigation of the competition between void coalescence and macroscopic strain localization using the periodic homogenization multiscale scheme. J. Mech. Phys. Solids 143, 104042. http://dx.doi.org/10.1016/j.jmps.2020.104042.

Zhu, J., Ben Bettaieb, M., Abed-Meraim, F., 2020b. Numerical investigation of necking in perforated sheets using the periodic homogenization approach. Int. J. Mech. Sci. 166, http://dx.doi.org/10.1016/j.ijmecsci.2019.105209.

Zhu, J.C., Ben Bettaieb, M., Abed-Meraim, F., 2022. Comparative study of three techniques for the computation of the macroscopic tangent moduli by periodic homogenization scheme. Eng. Comput. 38, 1365–1394. http://dx.doi.org/10.1007/s00366-020-01091-y.

Zhu, J.C., Ben Bettaieb, M., Abed-meraim, F., Huang, M.S., Li, Z.H., 2023a. Coupled effects of crystallographic orientation and void shape on ductile failure initiation using a CPFE framework. Eng. Fract. Mech. 280, 1–21. http://dx.doi.org/10.1016/j.engfracmech.2023.109121.

Zhu, J.C., Ben Bettaieb, M., Zhou, S., Abed-Meraim, F., 2023b. Ductility limit prediction for polycrystalline aggregates using a CPFEM-based multiscale framework. Int. J. Plast. 167, 103671. http://dx.doi.org/10.1016/j.ijplas.2023.103671.